Contributions to Mineralogy and Petrology (2022) 177:94
https://doi.org/10.1007/s00410-022-01955-0

ORIGINAL PAPER

# $Fe^{2+}$–Mg partitioning between olivine and liquid at low oxygen fugacity: an experimental and thermodynamic framework

**L. M. Saper[1,2] · M. B. Baker[1] · E. M. Stolper[1]**

Received: 23 December 2021 / Accepted: 8 August 2022 / Published online: 21 September 2022


## Abstract

A set of 1-atm gas-mixing experiments ($n = 31$) was run using Re wire loops at low-oxygen fugacity ($fO_2$, within one half-log unit of the Fe–FeO buffer) and temperatures of 1175–1400 °C to explore the compositional dependence of the $Fe^{2+}$–Mg olivine–liquid exchange coefficient, $K^{ol/liq}_{D,Fe^{2+}-Mg}$, under conditions where corrections for liquid $Fe^{3+}$ are small. The bulk compositions used for these experiments include a picrite, a high-alumina basalt, and a suite of three MORB compositions with variable Fe/Mg. The $K^{ol/liq}_{D,Fe^{2+}-Mg}$ values from the $n = 14$ experiments run on pre-saturated Re wire loops were fit to a regular solution model that relates $K^{ol/liq}_{D,Fe^{2+}-Mg}$ to temperature, melt composition, and olivine composition. $Fe^{2+}$–Mg exchange in the experiments is well-described using two parameters: the $SiO_2$ content of the liquid and the coexisting olivine composition. Combining our experiments with a literature compilation of low-pressure, low-$fO_2$ experiments (largely on non-terrestrial bulk compositions) produced a combined data set spanning a broad region of composition space (e.g., liquid $TiO_2$ and $Na_2O + K_2O$ contents up to 18.4 wt% and 8.4 wt%, respectively). Fitting this expanded experimental database required two additional liquid compositional terms: Ti, and a Si-(Na + K) cross-term. Because the $Fe^{3+}$ content of all of the experimental liquids is low, the compositional variation seen in $K^{ol/liq}_{D,Fe^{2+}-Mg}$ is effectively independent of the compositional effects on liquid $Fe^{3+}/Fe^{2+}$ ratios. Given olivine–liquid Mg or $Fe^{2+}$ partition coefficient information, it is possible to eliminate the explicit dependence of $K^{ol/liq}_{D,Fe^{2+}-Mg}$ on olivine composition, enabling a simple iterative approach for calculating the composition of coexisting olivine given only the bulk composition (and $Fe^{3+}/Fe^{2+}$ ratio) of an olivine-saturated liquid.

**Keywords** Experimental petrology · Olivine · Element partitioning · Thermodynamics

## Introduction

Experimental determinations of element partitioning between coexisting solid and liquid phases are essential for understanding crystallization and melting processes, such as modeling the chemical evolution of melts, their residues, and cumulate mushes. Olivine is the predominant mineral phase in the upper mantle (e.g., Stixrude and Lithgow-Bertelloni 2012; Warren 2016) and is the primary liquidus phase during low-pressure crystallization of primitive mafic melts (e.g., O'Hara 1968; Hess 1992; Grove and Brown 2018). Consequently, substantial effort has been devoted to quantifying chemical equilibrium between olivine and liquid (e.g., Bédard 2005), and in particular, the partitioning behavior of $Fe^{2+}$ and Mg (e.g., Longhi et al. 1978; Gee and Sack 1988; Toplis 2005; Putirka 2016). The goal of these studies was to provide a basis for modeling the melting of olivine-bearing mantle assemblages and for reconstructing basaltic liquid lines of descent. In addition, determining whether olivine–liquid pairs have approached equilibrium in experimental studies and in nature has often been based on measuring Fe and Mg in both phases, calculating a $Fe^{2+}$–Mg olivine–liquid exchange coefficient,

Communicated by Mark S. Ghiorso.

✉ L. M. Saper
Lee.Saper@ed.ac.uk

[1] Division of Geological and Planetary Sciences, California Institute of Technology, Pasadena, CA 91125, USA

[2] School of Geosciences, Grant Institute, University of Edinburgh, Edinburgh EH9 3FE, Scotland, UK

$$K^{ol/liq}_{D,Fe^{2+}-Mg} \equiv \frac{\left(\frac{X_{FeO}}{X_{MgO}}\right)^{ol}}{\left(\frac{X_{FeO}}{X_{MgO}}\right)^{liq}}, \quad (1)$$

and comparing it to an accepted $K^{ol/liq}_{D,Fe^{2+}-Mg}$ value. Equation (1) describes $Fe^{2+}$–Mg partitioning between olivine and silicate melt, where $X_{MgO}$ and $X_{FeO}$ are oxide mole fractions in the liquid and the olivine (Roeder and Emslie 1970; note that the oxide mole fractions in Eq. (1) can be replaced by oxide weight percents, $w_{MgO}$ and $w_{FeO}$). In Eq. (1), $X^{liq}_{FeO}$ refers to iron present in the liquid as $Fe^{2+}$ (we assume that all Fe in olivine is $Fe^{2+}$); later references to FeO* or Fe* refer to all iron ($Fe^{2+}$and $Fe^{3+}$) present in the liquid or in a bulk composition as $Fe^{2+}$. Hereafter, we only consider partitioning between olivine and liquid, and so the "ol/liq" specifier is dropped from "$K^{ol/liq}_{D,Fe^{2+}-Mg}$" and the $Fe^{2+}$–Mg olivine–liquid exchange coefficient is referred to as $K_{D,Fe^{2+}-Mg}$.

Applying $K_{D,Fe^{2+}-Mg}$ to petrological problems is rooted in the study of Roeder and Emslie (1970), who found that for Hawai'ian basalts equilibrated at atmospheric pressure and temperatures (T) of 1150–1300 °C, $K_{D,Fe^{2+}-Mg}$ is approximately constant with a value of 0.30. This value has been (and still is) widely used in the petrological literature (see Matzen et al. 2011 for re-evaluation of the original Roeder and Emslie 1970 data). However, it has long been recognized that 0.30 is only a convenient reference point and, as discussed below, that the exchange coefficient displays resolvable and systematic variations as a function of bulk composition. For example, experiments on high-Ti basaltic compositions showed that $K_{D,Fe^{2+}-Mg}$ is systematically lower than 0.30, decreasing to 0.22 in melts with up to 19 wt% $TiO_2$ (lunar basalts: Longhi et al. 1978; Grove and Beaty 1980; Delano 1980; Jones 1988; picrites at 1.2 and 2.8 GPa: Xirouchakis et al. 2001). Note that the experiments on lunar basalts were run under reducing conditions, often in Fe-metal capsules, thereby constraining $Fe^{3+}$ in the melt to low values and effectively eliminating the need to correct electron microprobe FeO* glass values for their $Fe^{3+}$ contents to calculate $K_{D,Fe^{2+}-Mg}$. Although Roeder (1974) found that the FeO contents of liquids saturated with Fe-metal and olivine decreased with increasing alkali and alumina contents, he concluded that $K_{D,Fe^{2+}-Mg}$ remained ~ 0.30 ± 0.03 in melts with up to 4.39 wt% $Na_2O$, 3.51 wt% $K_2O$, and 18.24 wt% $Al_2O_3$. Later work on six component basalts at low $fO_2$ demonstrated that liquids with elevated $Na_2O$ display systematically lower $K_{D,Fe^{2+}-Mg}$ values (e.g., down to 0.23 in melts with 7.5 wt% $Na_2O$; Shi 1993), consistent with experiments on natural alkalic basalts run at higher $fO_2$ near the fayalite–magnetite–quartz buffer (FMQ) (e.g., Gee and Sack 1988).

In addition to the effects of $TiO_2$, alkalis, and alumina, variations in the concentrations of major elements in the liquid (e.g., $SiO_2$: Longhi et al. 1978; Gee and Sack 1988; Toplis 2005; Putirka 2016; FeO + MgO: Kushiro and Walter 1998; Filiberto and Dasgupta 2011) and in the composition of the olivine (Toplis 2005; Blundy et al. 2020) have also been shown to correlate with variations in $K_{D,Fe^{2+}-Mg}$. As a result, several models have been developed to describe variations in $K_{D,Fe^{2+}-Mg}$ as functions of melt composition ± olivine composition ± T ± pressure (P) (e.g., Longhi et al. 1978; Ford et al. 1983; Gee and Sack 1988; Snyder and Carmichael 1992; Kushiro and Walter 1998; Kushiro and Mysen et al. 2002; Herzberg and O'Hara 2002; Toplis 2005; Filiberto and Dasgupta 2011; Putirka 2016; Blundy et al. 2020). Such models provide a more accurate description of olivine-melt equilibria than is possible by simply adopting a constant value for $K_{D,Fe^{2+}-Mg}$, and such descriptions are useful for applications including reconstructing primary melts (e.g., Herzberg and O'Hara 2002; Herzberg and Asimow 2015; Brown Krein et al. 2021), and correcting for post-entrapment crystallization in olivine-hosted melt inclusions (e.g., Danyushevsky et al. 2002; Gaetani and Watson 2002).

For melts coexisting with olivine, ferrous oxide in the quenched liquid (i.e., $FeO^{liq}$) must be known to calculate $K_{D,Fe^{2+}-Mg}$ from electron microprobe analyses that generally report all Fe as FeO*. $Fe^{3+}/Fe^{2+}$ ratios vary significantly over geologically relevant $fO_2$ values (e.g., Carmichael 1991; Cottrell et al. 2022 and references therein), thus the analyzed FeO* of natural or experimental glasses often requires a correction by subtracting the amount of $Fe^{3+}$ in the glass to obtain the $Fe^{2+}$ content. Only a relatively small number of experimental olivine–liquid pairs have direct measurements of $Fe^{3+}/Fe^{2+}$ in the quenched glasses, and for these, $K_{D,Fe^{2+}-Mg}$ can be calculated directly (Mysen and Dubinsky 2004; Partzsch et al. 2004; Mysen and Shang 2005; Mysen 2006, 2007; Matzen et al. 2011; Blundy et al. 2020; Waters et al. 2020). Most 1-atm experiments on terrestrial bulk composition have been done in the vicinity of the FMQ, where liquid FeO* is not a good approximation for $FeO^{liq}$. Thus, for these and other relatively oxidized experiments, the $Fe^{3+}/Fe^{2+}$ ratio of the melt must be calculated using one of the many algorithms that relate $Fe^{3+}/Fe^{2+}$ to melt composition, $fO_2$, and T (e.g., Sack et al. 1980; Kilinc et al. 1983; Kress and Carmichael 1988, 1991; Borisov and Shapkin 1989; Nikolaev et al. 1996; Jayasuriya et al. 2004; Ghiorso and Kress 2004; Putirka 2016; Borisov et al. 2018; O'Neill et al. 2018). For a given liquid composition at FMQ, the different $Fe^{3+}/Fe^{2+}$ parameterizations are not in agreement, and this leads to significant differences in calculated $K_{D,Fe^{2+}-Mg}$ values (see Matzen et al. 2011, Fig. 4); as shown in Supplementary Figure S1, these differences in calculated $Fe^{3+}/Fe^{2+}$ increase with increasing $fO_2$. Consequently, the need to correct for the presence of $Fe^{3+}$ in most

experimental glasses, particularly at $fO_2 > FMQ$, represents a source of uncertainty in reported $K_{D,Fe^{2+}-Mg}$ values (e.g., Matzen et al. 2011). For example, in experiments run over a wide range of $fO_2$, the fraction of $Fe^{2+}$ to Fe* in the melt can vary from > 95% (at very low $fO_2$, e.g., Bowen and Schairer 1935) to 20–30% (in air, e.g., Kress and Carmichael 1991; Jayasuriya et al. 2004; Mysen et al. 2004; Borisov et al. 2018), making it difficult to deconvolve the effects of melt and olivine composition on the $K_{D,Fe^{2+}-Mg}$ from our incomplete understanding of how melt composition and $fO_2$ affect the $Fe^{3+}/Fe^{2+}$ ratios of the liquids—a point emphasized by Blundy et al. (2020).

One way to circumvent the necessity of correcting for $Fe^{3+}$ in quenched glasses is to focus on experiments run under sufficiently reducing conditions such that nearly all the Fe present in the liquid is $Fe^{2+}$. For liquids, where $X_{FeO} \approx X_{FeO*}$, $K_{D,Fe^{2+}-Mg}$ can be determined with minimal correction from electron microprobe analyses of the glasses. Here, we present 1-atm experiments designed to generate olivine–liquid pairs at $fO_2$ within ± 0.5 log units of the iron–wüstite buffer (i.e., IW ± 0.5; buffer equation from Huebner 1971) using terrestrial basaltic compositions, which are underrepresented among previous experiments run at similarly reducing conditions. At $fO_2$ levels ≤ IW + 0.5, the concentration of FeO in the melt approaches that of FeO*. Importantly, absolute differences in $Fe^{3+}/Fe^{2+}$ ratios predicted by the available models at IW are also small (for a single composition, $Fe^{3+}/Fe^{2+}$ models predict a maximum difference of 2–4% absolute for our experiments). Thus, for such experiments, $K_{D,Fe^{*}-Mg}$ (referred to as $K_D$*, where $X^{liq}_{FeO}$ in Eq. (1) is replaced by $X^{liq}_{FeO*}$, see Eq. (2)) closely approaches $K_{D,Fe^{2+}-Mg}$, and correlations between liquid composition and $K_{D,Fe^{*}-Mg}$ can be used to isolate compositional effects on the partitioning of FeO and MgO between olivine and melt, independent of any $Fe^{3+}/Fe^{2+}$ correction. Combining our experimental data with low-$fO_2$ experiments from the literature, we present a thermodynamically based model to describe the compositional and temperature effects on $K_{D,Fe^{2+}-Mg}$ that spans most of the range of common terrestrial and extraterrestrial magmas.

## Methods

### Starting compositions

The bulk compositions used in this study are based on three basalt types [ocean island basalts (OIB); high-Al basalts (HAB); and mid-ocean ridge basalts (MORB)], and they were designed to have olivine as a liquidus phase and to span a range of Mg# (100[Mg/(Mg + Fe*)], molar). Bulk compositions are reported in Table 1. Mg# ranges from 40 to 80, and $SiO_2$, $TiO_2$, and $CaO/Al_2O_3$ values are 43.8–50.5 wt%, 0.55–1.41 wt%, and 0.65–0.81, respectively. SynHP1 is a synthetic, alkali-free picritic composition based on whole-rock compositions from Mauna Kea (see Matzen et al. 2011 and Table 1, this publication, for further details). As part of an earlier study, we had added $Cr_2O_3$ and $Mn_2O_3$ to synHP1 (the former to increase the stability field of spinel) to generate synHP1 + Cr + Mn (1.05 wt% $Cr_2O_3$ and 0.81 wt% MnO). All of the remaining bulk compositions have MnO contents of ~ 0.5 wt%; although this is higher than those typical of terrestrial basalts (0.1–0.2 wt%; e.g., Le Maitre 1976; Gale et al. 2013), we chose to elevate MnO concentrations to facilitate more precise determinations of Mn concentrations in olivine and melt without having to use a high microprobe beam current on the glasses. The HAB + Ol + Mn composition is a natural high-alumina basalt from Medicine Lake Highland (82–72c; Baker et al. 1991) to which 15% synthetic $Mg_2SiO_4$ powder was added to expand the olivine stability field to temperatures above 1300 °C (based on calculations using MELTS; Ghiorso and Sack 1995). The added forsterite resulted in a bulk composition with Mg# = 76 and the addition of $Mn_2O_3$ raised the MnO content from 0.16 to 0.49 wt%. In contrast to the synHP1 ± Cr + Mn compositions and the MORB compositions (discussed below) that are alkali-free, HAB + Ol + Mn has 1.88 wt% $Na_2O$ and 0.08 wt% $K_2O$.

To create the synthetic MORB-like compositions, we used the database of $Fo_{90}$-corrected mid-ocean-ridge segment average compositions from Gale et al. (2014) and fit each of the major and minor oxides as a linear function of MgO. An initial target composition (see notes to Table 1) was calculated by projecting these fits to an MgO value of 14 wt% (the mean and median MgO contents of the $Fo_{90}$-corrected compositions from Gale et al. 2014 are 13.8 and 13.9, respectively). This base composition has an Mg# of 73, ~ 14.4 wt% MgO when normalized to a sum of 100 wt% on an alkali- and MnO-free basis, and a molar sum of MgO + FeO* of 0.491. The bulk compositions synMORB80 (Mg# = 80) and synMORB60 (Mg# = 60) were generated by varying MgO/FeO* at constant molar MgO + FeO*, i.e., by varying MgO/FeO* until the bulk composition had an Mg# of either 80 or 60. MELTS calculations (Ghiorso and Sack 1995) at an $fO_2$ of IW + 0.5 using a bulk composition with Mg# = 40 derived in the manner described above predicted pigeonite as the liquidus phase, followed by plagioclase, and then olivine at T ~ 1100 °C. To expand the stability field for olivine in the synMORB40 composition, its total molar MgO + FeO* content was increased by a factor of 1.2 relative to synMORB80 and synMORB60 (molar sum of MgO + FeO* = 0.589, on an alkali- and MnO-free basis). MELTS calculations on this FeO* and MgO enriched composition predicted olivine as the primary liquidus phase at T = 1215 °C. Note that like the synHP1 and synHP1 + Cr + Mn bulk compositions, the synMORB compositions are alkali-free.

**Table 1** Bulk compositions of the starting mixes

| | synHP1[a] | synHP1 + Cr + Mn[b] | HAB + Ol + Mn | synMORB80[c] | synMORB60 | synMORB40 |
|---|---|---|---|---|---|---|
| $SiO_2$ | 45.39 | 44.57 | 47.14 | 50.66 | 48.97 | 43.78 |
| $TiO_2$ | 1.41 | 1.38 | 0.55 | 0.75 | 1.04 | 0.92 |
| $Al_2O_3$ | 8.28 | 8.47 | 15.49 | 14.08 | 13.61 | 12.17 |
| $Cr_2O_3$ | 0.22 | 1.05 | 0.03 | 0.00 | 0.00 | 0.00 |
| FeO* | 12.03 | 11.82 | 8.56 | 7.12 | 13.75 | 24.16 |
| MnO | 0.18 | 0.81 | 0.49 | 0.50 | 0.50 | 0.50 |
| MgO | 25.48 | 25.02 | 15.53 | 15.97 | 11.58 | 9.04 |
| CaO | 6.72 | 6.60 | 10.13 | 10.92 | 10.55 | 9.43 |
| $Na_2O$ | 0.00 | 0.00 | 1.88 | 0.00 | 0.00 | 0.00 |
| $K_2O$ | 0.00 | 0.00 | 0.08 | 0.00 | 0.00 | 0.00 |
| NiO | 0.29 | 0.29 | 0.08 | 0.00 | 0.00 | 0.00 |
| $P_2O_5$ | 0.00 | 0.00 | 0.04 | 0.00 | 0.00 | 0.00 |
| Total | 100 | 100 | 100 | 100 | 100 | 100 |
| Mg# | 79.1 | 79.1 | 76.4 | 80.0 | 60.0 | 40.0 |

Oxide concentrations are based on the mass fraction of components in each mix. FeO* = all Fe expressed as FeO. Mg# = 100 [Mg/(Mg + Fe)], molar. Note that HAB + Ol + Mn was the only natural basalt powder and was the only mix to which synthetic $Mg_2SiO_4$ was added. The remaining starting mixes were made of mixed oxides and $CaCO_3$ powders (see Starting Compositions). **a** From Matzen et al. (2011), Table 1 and Table 3 (the superliquidus experiments 43 and 34). The authors noted that the synHP1 mix had gained ~ 0.7 wt% $Al_2O_3$ during the grinding process, probably reflecting the fact that the grinding was done using an alumina mortar and pestle and that some fraction of the $Al_2O_3$ oxide powder had converted to corundum during repeated firings at 800–1000 °C. This increase in $Al_2O_3$ is included in the synHP1 composition reported above. **b** Mass balance of the synHP1 + Cr + Mn experiments showed a consistent increase in $Al_2O_3$ in the calculated bulk compositions relative to the nominal synHP1 + Cr + Mn composition; the average increase was ~ 3.3% and is most likely due to the same issue discussed in **(a),** since synHP1 + Cr + Mn was constructed using powder from the original batch of synHP1. The $Al_2O_3$ content of the nominal synHP1 + Cr + Mn composition has been increased by 0.31 wt%, the remaining oxide concentrations were reduced proportionally. **c** Initial target MORB composition based on $Fo_{90}$-corrected average subaqueous ridge segments from Gale et al. (2014), expressed in wt% on an alkali and MnO-free basis: $SiO_2$ = 50.2, $TiO_2$ = 1.07, $Al_2O_3$ = 13.95, FeO* = 9.54, MgO = 14.43, CaO = 10.81, Mg# = 73. The section Starting compositions describes how the compositions for the three synMORB mixes were calculated; for synMORB80, the weighed-out mass fraction of $TiO_2$ was low by ~ 30% (0.75 wt% instead of 1.07 wt%), all the remaining oxide concentrations were increased proportionally (note that these changes are quite small, e.g., silica changes from the original target value of 50.50 to 50.66 wt%). Drying temperatures to remove adsorbed water prior to weighing powders: $SiO_2$ and $TiO_2$ at 800 °C, $Al_2O_3$ at 1000 °C, $Fe_2O_3$ at 700 °C, $CaCO_3$ at 400 °C, and $Cr_2O_3$, $Mn_2O_3$, forsterite, and the synHP1 and HAB powders in a vacuum oven at 120 °C

High-purity oxides $SiO_2$, $TiO_2$, $Al_2O_3$, $Fe_2O_3$, $Mn_2O_3$, MgO, and $Cr_2O_2$, synthetic $Mg_2SiO_4$ powder, $CaCO_3$, and the preexisting synHP1 (synthetic) and HAB (natural basalt) powders were dried to remove adsorbed water prior to weighing to produce each of the bulk mixes (see caption to Table 1 for drying schedule). The powdered components were weighed, then ground and mixed under ethanol in an alumina mortar for at least 1 h. The homogenized powders were then pressed into ~ 1 cm diameter pellets under vacuum, with acetone as a binding agent.

## Experimental design

All experiments were run at 1 atm in a vertical Deltech furnace using $H_2$–$CO_2$ gas mixtures to control $fO_2$. The type-S thermocouple used to set the experimental run temperatures was calibrated at the melting point of gold. The $fO_2$ of the furnace atmosphere was set using a yttria-stabilized zirconia oxygen sensor, which was calibrated by bracketing the $fO_2$ of the IW reaction ($Fe + ½\ O_2 = FeO$) at 1350 °C—the bracketed reaction was found to lie within < 0.1 log units of the accepted value (Huebner 1971). Experiments were conducted at either IW + 0.5 or IW–0.5 (Table 2). Due to how the Re wire loop plus sample was introduced into the hot spot (see discussion below), the thermocouple and $fO_2$ sensor were not present in the furnace during the runs. The experimental $fO_2$ and T were thus set prior to each experiment, the furnace was run down to 1000 °C, and then the sample was introduced into the furnace which was run up to the target T based on the relationship between hotspot temperature and the set point temperature. For experiments at T ≥ 1225 °C, the $fO_2$ was set at the experimental run temperature; for the experiments at 1175 °C, the appropriate $H_2$/$CO_2$ ratio in the gas was set with the furnace hotspot held at

**Table 2** Experimental run conditions and products

| Name | Starting Mix | Run Type | Time (hr) | T °C | $\log_{10}fO_2$ | ΔIW | Re[a] Loop # | Phases[b] | ΔFeO (%)[c] | $K_{D,Fe^*-Mg}^{ol/liq}$ [d] | 1σ[e] | $K_{D,Fe^{2+}-Mg}^{ol/liq}$ [f] |
|---|---|---|---|---|---|---|---|---|---|---|---|---|
| RKD-1 | synHP1 + Cr + Mn | S | 6 | 1350 | –9.7 | +0.5 | 1 | ol, gl, sp, Re | –1.29 | 0.3124 | 0.0089 | 0.3247 |
| RKD-2 | synHP1 + Cr + Mn | S | 17 | 1350 | –9.7 | +0.5 | 2 | ol, gl, sp, Re | –10.32 | 0.3133 | 0.0102 | 0.3257 |
| RKD-3 | synHP1 + Cr + Mn | S | 17 | 1350 | –9.7 | +0.5 | 3 | ol, gl, sp | –12.90 | 0.3133 | 0.0040 | 0.3253 |
| RKD-4 | synHP1 + Cr + Mn | S | 42 | 1350 | –9.7 | +0.5 | 4 | ol, gl, sp, (met) | –13.43 | 0.3108 | 0.0031 | 0.3225 |
| RKD-5 | synHP1 + Cr + Mn | E | 19 | 1350 | –9.7 | +0.5 | 4 | ol, gl, sp | –5.77 | 0.3154 | 0.0039 | 0.3273 |
| RKD-6 | synHP1 + Cr + Mn | E | 17 | 1300 | –10.2 | +0.5 | 4 | ol, gl, sp, (met) | –1.74 | 0.3152 | 0.0029 | 0.3262 |
| RKD-7 | synHP1 + Cr + Mn | E | 17 | 1400 | –9.2 | +0.5 | 4 | ol, gl, sp | –6.52 | 0.3158 | 0.0038 | 0.3286 |
| RKD-8 | HAB + Ol + Mn | S | 17 | 1300 | –10.2 | +0.5 | 5 | ol, gl | –1.24 | 0.3003 | 0.0034 | 0.3110 |
| RKD-9 | HAB + Ol + Mn | S | 48 | 1300 | –10.2 | +0.5 | 5 | ol, gl | –7.34 | 0.3031 | 0.0034 | 0.3134 |
| RKD-12 | HAB + Ol + Mn | E | 24 | 1300 | –10.2 | +0.5 | 5 | ol, gl | –4.06 | 0.3038 | 0.0047 | 0.3144 |
| RKD-13 | synMORB Mg80 | S | 20 | 1300 | –10.2 | +0.5 | 6 | ol, gl, (met) | –3.94 | 0.3174 | 0.0030 | 0.3275 |
| RKD-14 | synMORB Mg80 | E | 24 | 1300 | –10.2 | +0.5 | 6 | ol, gl, (met) | –4.37 | 0.3149 | 0.0034 | 0.3249 |
| RKD-15 | synMORB Mg80 | E | 23 | 1225 | –11.1 | +0.5 | 6 | ol, gl, px, pl, (met) | –1.76 | 0.3155 | 0.0044 | 0.3247 |
| RKD-16 | synMORB Mg60 | S | 24 | 1225 | –11.1 | +0.5 | 7 | ol, gl, (met) | –3.70 | 0.3249 | 0.0036 | 0.3352 |
| RKD-17 | synMORB Mg60 | E | 24 | 1225 | –11.1 | +0.5 | 7 | ol, gl, (met) | –2.96 | 0.3247 | 0.0035 | 0.3350 |
| RKD-19 | HAB + Ol + Mn | S | 48 | 1225 | –11.1 | +0.5 | 5 | ol, gl, pl | –5.60 | 0.3042 | 0.0069 | 0.3140 |
| RKD-20 | HAB + Ol + Mn | E | 48 | 1225 | –11.1 | +0.5 | 5 | ol, gl, pl | –6.45 | 0.3073 | 0.0049 | 0.3172 |
| RKD-21 | synMORB Mg60 | E | 48 | 1175 | –11.7 | +0.5 | 7 | ol, gl, px, pl, (met) | –1.19 | 0.3284 | 0.0049 | 0.3394 |
| RKD-22 | synMORB Mg40 | S | 48 | 1175 | –11.7 | +0.5 | 6 | ol, gl, pl, (met) | 1.42 | 0.3489 | 0.0035 | 0.3617 |
| RKD-23 | synMORB Mg40 | S | 25 | 1175 | –11.7 | +0.5 | 9 | ol, gl, pl, (met) | –0.88 | 0.3354 | 0.0057 | 0.3477 |
| RKD-24 | synMORB Mg40 | E | 48 | 1175 | –11.7 | +0.5 | 9 | ol, gl, pl, (met) | –0.50 | 0.3387 | 0.0034 | 0.3511 |
| RKD-25 | synHP1 | E | 48 | 1350 | –9.7 | +0.5 | 4 | ol, gl | –8.31 | 0.3146 | 0.0036 | 0.3262 |
| RKD-26 | synHP1 + Cr + Mn | E | 48 | 1300 | –10.2 | +0.5 | 4 | ol, gl, sp | –5.59 | 0.3157 | 0.0026 | 0.3266 |
| RKD-28 | synMORB Mg80 | S | 24 | 1300 | –11.2 | –0.5 | 10 | ol, gl, (met) | –5.47 | 0.3180 | 0.0035 | 0.3242 |
| RKD-29 | synMORB Mg80 | S | 22 | 1300 | –11.2 | –0.5 | 10 | ol, gl, (met) | –5.96 | 0.3136 | 0.0033 | 0.3197 |
| RKD-30 | synMORB Mg80 | E | 24 | 1300 | –11.2 | –0.5 | 10 | ol, gl, (met) | –5.41 | 0.3174 | 0.0032 | 0.3237 |
| RKD-31 | synMORB Mg40 | S | 24 | 1175 | –12.7 | –0.5 | 11 | ol, gl, pl, (met) | –0.64 | 0.3358 | 0.0069 | 0.3433 |
| RKD-32 | synMORB Mg40 | S | 24 | 1175 | –12.7 | –0.5 | 11 | ol, gl, pl, (met) | –0.96 | 0.3344 | 0.0046 | 0.3418 |
| RKD-33 | synMORB Mg40 | S | 48 | 1175 | –12.7 | –0.5 | 12 | ol, gl, pl, (met) | –1.60 | 0.3459 | 0.0034 | 0.3536 |
| RKD-34 | synMORB Mg40 | S | 24 | 1175 | –12.7 | –0.5 | 12 | ol, gl, pl, (met) | –0.61 | 0.3270 | 0.0041 | 0.3344 |
| RKD-35 | synMORB Mg40 | E | 48 | 1175 | –12.7 | –0.5 | 12 | ol, gl, pl, (met) | –1.25 | 0.3500 | 0.0040 | 0.3578 |

Compositions of the starting mixes are listed in Table 1. ΔIW refers to the $fO_2$ of the experiments expressed in log units relative to the iron–wüstite buffer reaction calculated at the experimental T and 1 atm (Huebner 1971). Saturation experiments (S) were those used to precondition wire loops; equilibration experiments (E) were run using the pre-saturated loops. **a** Re loop number used in each experiment. **b** Phase abbreviations: ol – olivine, gl – glass, sp – spinel, px – pyroxene, pl – plagioclase, Re – Re metal globules, which were only observed in RKD-1 and RKD-2 due to initial oxidation of the metal (see Supplementary Section S2), and (met) – Fe–Pt metal blebs, which were observed as trace contaminants (labeled in parentheses) in 19 experiments, but maybe present in all of the runs; see Fe–Pt metal blebs and Supplementary Section S1.4. **c** ΔFeO* is the percent change in bulk FeO* calculated by mass balance (see Approach to equilibrium and Supplementary Section S3. **d** $K_{D,Fe^*-Mg}^{ol/liq} = (FeO/MgO)^{ol} / (FeO^*/MgO)^{liq}$ and is calculated using the averages of olivine and glass analyses in each experiment (Table 3). **e** 1σ calculated by summing the errors in FeO* and MgO in each phase in quadrature. **f** $K_{D,Fe^{2+}-Mg}^{ol/liq}$, where $Fe^{3+}/Fe^{2+}$ in the glass is calculated using the expression of Borisov et al. (2018)

1250 °C to ensure that the gas mixture was in equilibrium (Beckett and Mendybaev 1997), then at 1175 °C the gas mixture was adjusted slightly to achieve the correct $fO_2$.

For each experiment, an ~ 80–100 mg chip was removed from the pellet of a given starting composition and attached to a Re wire loop using polyvinyl alcohol. The Re loop and sample were suspended from thin Pt quench wire attached to two 0.039″ diameter Pt wires within a two-hole ceramic rod. Given that Re is volatile in an oxidizing atmosphere at high temperatures (i.e., $fO_2 >$ FMQ; Borisov and Jones 1999) and that the furnace tube was initially filled with air, the ceramic rod was positioned so that the loop and sample were at the top (and cool) part of the furnace tube when inserted into the furnace. With the controller set at 1000 °C, the $H_2$–$CO_2$ gas mixture was then introduced into the sealed furnace tube and allowed to equilibrate for ~ 30 min. The Re loop was then slowly lowered into the hot spot over the following 20 to 30 min. Once the silicate chip was positioned in the hotspot, the furnace was ramped up to the target run temperature at a rate of ~ 10 °C/min. The experiments were then held isothermally at temperatures of 1175–1400 °C for 6–48 h. All experiments were terminated by electrically fusing the thin Pt hanging wire and dropping the silicate and wire loop into deionized water. Temperature, run time, $fO_2$, and other notes on particular experiments are reported in Table 2. After quenching, the silicate bead was removed from the wire loop by gently tapping it with a small-diameter drill blank and hammer—this was sufficient to remove nearly all of the silicate material from the loop.

In the T-$fO_2$ region where Re is stable, it alloys with Fe to a much lesser extent than Pt (e.g., Grove 1982; Borisov and Jones 1999; Kessel et al. 2001). Nevertheless, at $fO_2 \lesssim$ IW + 1, Fe-loss to a Re sample container becomes non-trivial (Borisov and Jones, 1999). For this reason, the Re loops were preconditioned for each bulk composition and $fO_2$ by running one or two "saturation" experiments for each loop (denoted "S" in Table 2). The preconditioned Re loops were then reused for one or more subsequent experiments, and those experiments are referred to as "equilibration" experiments ("E" in Table 2), which were the only experiments used in modeling $K_{D,Fe^{2+}-Mg}$ (see Discussion). The loop number used for each experiment is listed in Table 2, along with the experimentally produced phases, and the % change in bulk FeO* as determined by mass balance (see Approach to equilibrium). The acronym used for our low-$fO_2$ experiments is "RKD", which stands for Reduced $K_D$.

## Analytical techniques

Chips of silicate material recovered from each experiment were mounted in epoxy, ground down with alumina papers, polished with < 2 µm and 0.25 µm diamond powder, and then ultrasonicated in ethanol. All experiments and secondary standards were carbon coated at the same time to ensure that they had the same carbon-coat thickness. Quantitative wavelength-dispersive (WDS) analyses of glasses, silicates, and oxides were collected with a JEOL JXA-8200 electron microprobe at Caltech operating at an accelerating voltage of 15 keV. Backgrounds on primary standards, secondary standards, and unknowns were determined using the mean-atomic-number procedure of Donovan and Tingle (1996) and raw X-ray counts were reduced with a modified ZAF procedure (Armstrong 1988). See Table 3 for a list of primary standards and count times for each analyzed element. Glasses were analyzed using a 10 nA beam current, and a 10 µm diameter beam. Glass analyses with oxide sums of 100 ± 1.5% were considered acceptable. Olivines were analyzed using a 40 nA beam current with a 1 µm diameter beam; olivine analyses were accepted if they had analytical totals of 100 ± 1.5%, a tetrahedral cation sum of 1.000 ± 0.015, and an octahedral cation sum of 2.000 ± 0.015, both calculated on a four-oxygen basis (Supplementary Figure S2). Spinels were analyzed using a 10 nA beam current and a focused beam (< 1 µm) due to their small size, typically < 10 µm across. The $Fe^{3+}/Fe^{2+}$ values of the spinels were calculated assuming ideal stoichiometry. Because all of the spinel analyses contained between 0.2 and 0.6 wt% $SiO_2$, likely due to Si contamination from beam interaction with the surrounding glass or olivine (e.g., Matzen et al. 2011; Davis and Cottrell 2018 and references therein), we corrected the spinel analyses following the procedure discussed in Matzen et al. (2011). A 10 nA and 1 µm beam was used to analyze plagioclase and pyroxene; analyses were accepted if the oxide sum was 100 ± 2%, and the cation sums for plagioclase and pyroxene were 5.00 ± 0.02 per 8 oxygens and 4.00 ± 0.05 per 6 oxygens, respectively. Analyses of metal (see section Fe–Pt metal blebs) used a focused 25 nA beam, along with pure metal standards and off-peak backgrounds (Supplementary Section S1.4).

Euhedral olivine grains > 20 µm in longest dimension were selected for analysis and analyses of the rims were taken within 2–5 µm of the crystal edge. The cores in a subset of olivine grains from each experiment were also analyzed to check for compositional zoning. Due to stage drift and beam alignment issues, some rim analyses have $Al_2O_3$ contents higher than those expected in olivine phenocrysts (e.g., Sobolev et al. 2007). These elevated values are most likely due to X-ray counts from the adjacent glass. The alumina contents in olivine cores from each of the experiments showed limited variation, with typical 1σ values of ~ 0.01 wt%. For a given experiment, we used the maximum alumina content in the olivine core analyses plus 0.01 wt% $Al_2O_3$ to define the maximum acceptable alumina content in rim compositions from the same experiment. For example, in runs RKD-5 and RKD-14, the maximum alumina core values were 0.07 and 0.03 wt%, respectively, and thus

**Table 3** Experimental glass and olivine rim compositions in wt%

| Name | Phase | n | $SiO_2$ | $TiO_2$ | $Al_2O_3$ | $Cr_2O_3$ | FeO* | MnO | MgO | CaO | $Na_2O$ | $K_2O$ | NiO | Totals |
|---|---|---|---|---|---|---|---|---|---|---|---|---|---|---|
| RKD-1 | gl | 46 | 47.2(4) | 1.93(1) | 11.2(1) | 0.5(2) | 11.64(23) | 0.86(3) | 15.29(28) | 9.3(1) | 0.72(4) | 0.04(1) | | 98.92 |
| | ol | 20 | 39.4(4) | 0.01(2) | 0.10(2) | 0.44(2) | 11.33(9) | 0.67(1) | 47.62(22) | 0.30(2) | | | | 99.88 |
| RKD-2 | gl | 48 | 47.8(4) | 1.9(2) | 11.5(2) | 0.52(2) | 10.48(23) | 0.84(2) | 15.18(21) | 9.5(1) | 1.13(4) | 0.07(1) | | 99.05 |
| | ol | 25 | 39.2(6) | 0.01(1) | 0.10(2) | 0.45(2) | 10.55(18) | 0.68(1) | 48.79(52) | 0.30(1) | | | | 100.11 |
| RKD-3 | gl | 20 | 48.0(1) | 1.95(3) | 12.2(1) | 0.50(2) | 10.14(8) | 0.82(2) | 14.63(8) | 9.54(3) | 1.04(5) | 0.07(1) | 0.02(2) | 98.99 |
| | ol | 15 | 40.1(3) | 0.05(3) | 0.09(1) | 0.44(4) | 10.20(8) | 0.67(1) | 46.96(18) | 0.30(1) | | | 0.17(2) | 99.00 |
| RKD-4 | gl | 20 | 47.9(2) | 1.96(3) | 12.4(1) | 0.55(4) | 10.11(6) | 0.85(3) | 14.71(9) | 9.54(3) | 0.69(4) | 0.064(4) | 0.01(1) | 98.82 |
| | ol | 10 | 40.3(1) | 0.05(1) | 0.08(1) | 0.44(2) | 10.07(4) | 0.66(1) | 47.14(11) | 0.28(1) | | | 0.14(1) | 99.19 |
| RKD-5 | gl | 20 | 48.2(1) | 1.95(2) | 12.09(4) | 0.56(2) | 11.13(7) | 0.87(2) | 14.97(10) | 9.48(2) | 0.48(4) | 0.04(1) | 0.06(2) | 99.78 |
| | ol | 15 | 40.0(3) | 0.05(1) | 0.08(1) | 0.44(2) | 10.97(9) | 0.68(1) | 46.79(17) | 0.27(1) | | | 0.33(2) | 99.59 |
| RKD-6 | gl | 18 | 48.6(1) | 2.14(3) | 13.3(1) | 0.40(2) | 10.93(5) | 0.85(2) | 12.53(8) | 10.39(4) | 0.35(3) | 0.03(1) | 0.08(2) | 99.58 |
| | ol | 12 | 39.6(1) | 0.04(1) | 0.07(1) | 0.34(1) | 12.42(4) | 0.74(1) | 45.18(15) | 0.28(1) | | | 0.53(2) | 99.24 |
| RKD-7 | gl | 19 | 47.1(1) | 1.78(3) | 11.2(1) | 0.74(2) | 11.37(8) | 0.86(3) | 17.51(15) | 8.65(4) | 0.29(4) | 0.04(1) | 0.04(2) | 99.55 |
| | ol | 12 | 40.0(2) | 0.04(1) | 0.09(1) | 0.50(2) | 9.74(3) | 0.60(1) | 47.48(17) | 0.27(1) | | | 0.22(1) | 98.91 |
| RKD-8 | gl | 20 | 47.9(1) | 0.60(2) | 17.8(1) | 0.03(1) | 8.26(5) | 0.49(2) | 11.84(8) | 11.29(3) | 1.6(1) | 0.08(1) | 0.03(1) | 99.90 |
| | ol | 7 | 40.0(2) | 0.01(1) | 0.08(1) | 0.03(1) | 9.95(7) | 0.47(1) | 47.54(12) | 0.36(1) | | | 0.28(1) | 98.71 |
| RKD-9 | gl | 20 | 48.3(1) | 0.60(2) | 18.0(1) | 0.03(1) | 7.78(6) | 0.48(2) | 12.36(7) | 11.28(3) | 1.00(4) | 0.07(1) | 0.02(1) | 99.90 |
| | ol | 11 | 40.3(2) | 0.01(1) | 0.07(2) | 0.02(1) | 9.21(5) | 0.45(1) | 48.30(14) | 0.32(1) | | | 0.16(2) | 98.85 |
| RKD-12 | gl | 15 | 48.4(1) | 0.60(2) | 17.72(5) | 0.03(1) | 8.11(6) | 0.49(2) | 12.41(4) | 11.33(2) | 1.34(5) | 0.08(1) | 0.02(2) | 100.58 |
| | ol | 15 | 40.5(1) | 0.01(1) | 0.07(2) | 0.03(1) | 9.58(12) | 0.46(1) | 48.25(18) | 0.34(1) | | | 0.20(2) | 99.38 |
| RKD-13 | gl | 20 | 51.2(1) | 0.79(1) | 15.5(1) | | 6.76(4) | 0.48(2) | 13.42(5) | 11.64(4) | 0.34(3) | 0.02(1) | | 100.12 |
| | ol | 14 | 40.8(2) | 0.02(1) | 0.05(2) | | 7.94(4) | 0.42(1) | 49.66(15) | 0.30(1) | | | | 99.25 |
| RKD-14 | gl | 20 | 51.2(1) | 0.80(2) | 15.4(1) | | 6.75(4) | 0.49(2) | 13.51(7) | 11.77(3) | 0.27(3) | 0.02(1) | | 100.24 |
| | ol | 10 | 41.2(1) | 0.02(1) | 0.04(1) | | 7.88(5) | 0.42(1) | 50.09(15) | 0.30(1) | | | | 99.94 |
| RKD-15 | gl | 20 | 52.2(1) | 1.07(3) | 15.6(1) | | 7.24(5) | 0.51(2) | 10.16(06) | 12.89(4) | 0.13(3) | 0.008(4) | | 99.79 |
| | ol | 10 | 40.4(3) | 0.02(1) | 0.04(2) | | 10.65(10) | 0.54(1) | 47.38(21) | 0.34(1) | | | | 99.38 |
| RKD-16 | gl | 21 | 50.6(2) | 1.06(2) | 14.6(1) | | 12.98(7) | 0.50(2) | 9.59(05) | 11.25(3) | 0.11(2) | 0.00 | | 100.65 |
| | ol | 7 | 39.3(2) | 0.02(1) | 0.03(1) | | 18.28(15) | 0.52(2) | 41.56(12) | 0.31(1) | | | | 100.05 |
| RKD-17 | gl | 20 | 50.0(2) | 1.08(2) | 14.8(1) | | 13.04(8) | 0.50(2) | 9.53(06) | 11.31(3) | 0.09(2) | 0.006(4) | | 100.43 |
| | ol | 14 | 39.0(2) | 0.02(1) | 0.04(1) | | 18.33(10) | 0.51(1) | 41.28(13) | 0.32(2) | | | | 99.53 |
| RKD-19 | gl | 19 | 51.6(3) | 1.02(2) | 16.2(2) | 0.03(1) | 8.87(10) | 0.60(2) | 8.84(16) | 12.1(1) | 1.42(4) | 0.12(1) | 0.01(1) | 100.82 |
| | ol | 8 | 40.3(1) | 0.03(1) | 0.04(1) | 0.04(1) | 13.77(9) | 0.70(1) | 45.09(16) | 0.39(1) | | | 0.21(1) | 100.59 |
| RKD-20 | gl | 14 | 51.2(1) | 0.99(2) | 16.5(1) | 0.04(1) | 8.69(8) | 0.60(2) | 9.11(06) | 12.14(4) | 1.35(3) | 0.11(1) | 0.01(1) | 100.69 |
| | ol | 12 | 40.3(2) | 0.03(1) | 0.05(1) | 0.04(1) | 13.33(14) | 0.68(1) | 45.44(13) | 0.38(1) | | | 0.19(1) | 100.42 |
| RKD-21 | gl | 19 | 48.7(2) | 2.04(3) | 13.0(1) | | 16.28(10) | 0.58(2) | 6.90(05) | 12.14(5) | 0.22(2) | 0.01(1) | | 99.93 |
| | ol | 5 | 37.2(4) | 0.03(2) | 0.09(3) | | 26.44(13) | 0.75(3) | 34.12(34) | 0.45(3) | | | | 99.14 |
| RKD-22 | gl | 20 | 45.0(1) | 1.10(2) | 13.3(1) | | 23.44(12) | 0.51(3) | 5.92(04) | 10.66(2) | 0.08(2) | 0.01(1) | | 100.02 |
| | ol | 15 | 35.1(1) | 0.04(1) | 0.05(1) | | 36.31(14) | 0.66(1) | 26.28(12) | 0.47(3) | | | | 98.92 |
| RKD-23 | gl | 19 | 45.3(1) | 1.09(2) | 12.88(4) | | 23.18(9) | 0.51(2) | 6.00(05) | 10.60(3) | 0.07(2) | 0.004(4) | | 99.63 |
| | ol | 13 | 35.8(2) | 0.03(1) | 0.03(1) | | 35.51(35) | 0.64(1) | 27.43(30) | 0.43(3) | | | | 99.86 |
| RKD-24 | gl | 20 | 45.4(1) | 1.11(2) | 13.1(1) | | 23.34(11) | 0.53(1) | 6.03(04) | 10.54(3) | 0.08(2) | 0.01(1) | | 100.07 |
| | ol | 12 | 35.5(2) | 0.03(1) | 0.04(1) | | 35.64(14) | 0.64(1) | 27.20(11) | 0.41(2) | | | | 99.44 |
| RKD-25 | gl | 19 | 48.7(1) | 2.07(3) | 12.5(1) | 0.24(1) | 11.09(7) | 0.17(2) | 15.15(8) | 10.02(4) | 0.34(3) | 0.04(1) | 0.05(2) | 100.34 |
| | ol | 17 | 40.5(3) | 0.04(1) | 0.059(4) | 0.17(1) | 11.01(7) | 0.14(1) | 47.76(22) | 0.26(1) | | | 0.29(2) | 100.24 |
| RKD-26 | gl | 20 | 49.4(1) | 2.10(3) | 13.0(1) | 0.43(2) | 10.71(6) | 0.84(3) | 13.10(6) | 10.32(2) | 0.25(2) | 0.03(1) | 0.05(2) | 100.29 |
| | ol | 13 | 40.5(1) | 0.04(1) | 0.059(4) | 0.35(1) | 11.91(4) | 0.72(1) | 46.16(12) | 0.26(1) | | | 0.42(1) | 100.38 |
| RKD-28 | gl | 20 | 51.5(1) | 0.80(2) | 15.75(6) | | 6.67(4) | 0.50(2) | 13.36(4) | 11.79(2) | 0.21(2) | 0.02(1) | | 100.63 |
| | ol | 15 | 41.0(3) | 0.02(1) | 0.04(1) | | 7.96(6) | 0.42(1) | 50.08(17) | 0.29(1) | | | | 99.73 |
| RKD-29 | gl | 20 | 51.8(1) | 0.78(2) | 15.52(7) | | 6.70(5) | 0.49(2) | 13.76(5) | 11.74(4) | 0.28(2) | 0.02(1) | | 101.07 |
| | ol | 19 | 41.3(2) | 0.02(1) | 0.04(1) | | 7.72(5) | 0.41(1) | 50.58(14) | 0.30(1) | | | | 100.37 |

**Table 3** (continued)

| Name | Phase | n | $SiO_2$ | $TiO_2$ | $Al_2O_3$ | $Cr_2O_3$ | FeO* | MnO | MgO | CaO | $Na_2O$ | $K_2O$ | NiO | Totals |
|---|---|---|---|---|---|---|---|---|---|---|---|---|---|---|
| RKD-30 | gl | 20 | 51.5(1) | 0.75(2) | 15.19(7) | | 6.75(5) | 0.50(2) | 14.34(6) | 11.54(4) | 0.23(2) | 0.02(1) | | 100.79 |
| | ol | 18 | 41.1(2) | 0.02(1) | 0.04(1) | | 7.57(4) | 0.40(1) | 50.67(12) | 0.30(2) | | | | 100.09 |
| RKD-31 | gl | 21 | 45.1() | 1.03(2) | 13.47(6) | | 22.88(8) | 0.52(2) | 6.36(5) | 10.61(3) | 0.05(2) | 0.006(4) | | 100.02 |
| | ol | 17 | 36.1(2) | 0.05(1) | 0.04(1) | | 34.43(43) | 0.62(2) | 28.49(41) | 0.41(4) | | | | 100.13 |
| RKD-32 | gl | 21 | 45.1(1) | 1.02(2) | 13.47(6) | | 22.54(12) | 0.51(2) | 6.37(4) | 10.56(2) | 0.04(2) | 0.004(4) | | 99.63 |
| | ol | 6 | 36.0(2) | 0.04(1) | 0.04(2) | | 33.89(29) | 0.60(1) | 28.67(20) | 0.42(1) | | | | 99.62 |
| RKD-33 | gl | 20 | 45.5(1) | 1.03(2) | 13.50(6) | | 22.47(12) | 0.51(2) | 6.52(4) | 10.56(2) | 0.06(2) | 0.005(4) | | 99.98 |
| | ol | 13 | 36.2(2) | 0.04(1) | 0.04(1) | | 34.42(12) | 0.62(1) | 28.42(12) | 0.42(2) | | | | 100.13 |
| RKD-34 | gl | 20 | 44.9(1) | 1.07(3) | 13.42(6) | | 22.78(9) | 0.52(2) | 6.25(5) | 10.65(2) | 0.05(2) | 0.01(1) | | 99.74 |
| | ol | 17 | 36.1(3) | 0.04(1) | 0.04(2) | | 34.18(21) | 0.62(1) | 28.56(19) | 0.42(3) | | | | 99.96 |
| RKD-35 | gl | 20 | 45.0(1) | 1.07(2) | 13.55(6) | | 22.32(1) | 0.50(2) | 6.40(4) | 10.57(2) | 0.07(3) | 0.005(4) | | 99.47 |
| | ol | 16 | 35.8(2) | 0.03(1) | 0.04(1) | | 34.42(22) | 0.62(1) | 28.21(18) | 0.42(3) | | | | 99.58 |

Reported values correspond to the mean composition of each phase measured in each experiment; the numbers in parentheses correspond to one standard deviation in terms of the least unit cited, i.e., 11.64(23) = 11.64 ± 0.23(1σ), or 11.33(9) = 11.33 ± 0.09(1σ). gl – glass, ol – olivine. *n* = number of analyses that were used to calculate averages and standard deviations. All olivine compositions come from analyses of olivine rims. The following primary standards were used: Si – for olivine, forsterite; for glass, VG-2, Ti – $TiO_2$, Al – for olivine, $Al_2O_3$; for glass, VG-2, Cr – $Cr_2O_3$, Fe – fayalite, Mn – tephroite, Mg – forsterite, Ca – for olivine, anorthite; for glass, VG-2, Na – albite, K – microcline, Ni – NiO. The Mean Atomic Number (MAN) protocol was used to calculate backgrounds. On-peak counting times were as follows: Si – 70 s, Ti – 60 s, Al – 100 s, Cr – 70 s, Fe – 50 s, Mn – 40 s, Mg – 50 s, Ca – 100 s, Na – 20 s, K –20 s, Ni – 30 s. Note that the olivines and glasses in RKD-1 and RKD-2 were measured using a different analytical protocol than the remaining experiments (count times were shorter) and NiO was not analyzed in this session. The count times for these two experiments were as follows: Si – 30 s, Ti – 30 s, Al – 30 s, Cr – 30 s, Fe – 25 s, Mn – 30 s, Mg – 30 s, Ca – 30 s, Na – 20 s, K – 20 s, Ni – not analyzed

olivine rim analyses with > 0.08 wt% and > 0.04 wt% $Al_2O_3$ were rejected. Thus, all olivine rim compositions used to generate the averages listed in Table 3 were subjected to three filters: oxide sum, stoichiometry, and $Al_2O_3$ content.

Secondary standards were used to assess the accuracy and precision of Fe/Mg ratios, and to monitor instrumental drift within an analytical session and between sessions. Three secondary standard glasses were used (BHVO-2g, BIR-1g, and GOR-128g) as well as two olivines from Caltech's mineral collection (San Carlos, CIT–SC, and Guadalupe Island, CIT–GI). To monitor instrumental drift, the secondary standards were measured before and after measuring a particular phase in each equilibration experiment; e.g., the same glass chip of each secondary glass standard was measured 2–3 times before and after the 14–20 glass analyses of each equilibration experiment. A similar procedure (using the olivine secondary standards) was applied to analyzing the olivines in the equilibration experiments.

## Results

Average compositions of spinel, plagioclase, pyroxene, and rare Fe–Pt blebs (interpreted to be a contaminant; see below) are reported in the Supplement (Section S1 and Supplementary Table S1). Although spinel, plagioclase, and pyroxene were used in the mass balance calculations (see Approach to equilibrium), they are not discussed further here.

### Glass and olivine

For each of the saturation and equilibration experiments, the glass and olivine rim analyses that passed the various quality filters were averaged to obtain mean compositions (listed in Table 3); the number of analyses ranged from 14 to 48 for the glasses and 5 to 25 for the olivines. Standard deviations (Table 3) refer to the distribution of multiple microprobe analyses of each phase in each experiment (i.e., not to the standard error of the mean), and unless specified otherwise, references to standard deviations and the use of the ± symbol in the text refers to 1σ errors.

Figure 1 shows variations in the wt% concentrations of liquid $SiO_2$ and $Al_2O_3$ as a function of MgO and variations in glass Mg# as a function of run temperature. MgO contents range from ~ 6 to 17.5 wt% and $SiO_2$ and $Al_2O_3$ vary from 45 to 52 wt% (Fig. 1A) and from 11 to 18 wt% (Fig. 1B), respectively. The Mg#s of the glasses range from 31.5 to 78.1, and they are higher in experiments run on the same bulk composition at higher T (Fig. 1C). Variations in other oxide concentrations include: $TiO_2$ from 0.6 to 2.14 wt%, CaO from 8.6 to 13 wt%, and $Na_2O + K_2O$ from 0.04 to 1.65 wt%. All of the experimental glasses are hypersthene normative (calculated using the CIPW norm, all Fe as FeO*). The fact that all experiments, including those on the alkali-free synHP1, synHP1 + Cr + Mn, and synMORB bulk compositions, contained some Na and K can be attributed to the gradual depletion of contaminant Na + K on the inner wall of

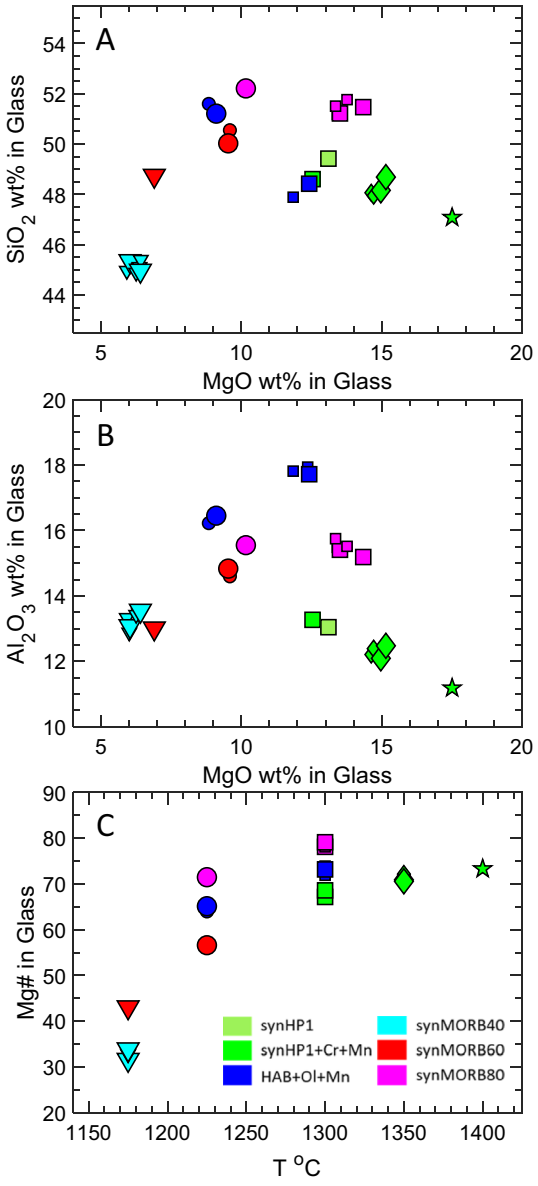


**Fig. 1** Compositional trends in experimental glasses. **A** wt% $SiO_2$ vs. wt% MgO in the glasses, **B** wt% $Al_2O_3$ vs. wt% MgO, **C** Mg# (100[Mg/(Mg + Fe)], molar) in the experimental glasses vs. experimental T (°C). Larger symbols are equilibration experiments (labeled E in Table 2); smaller symbols are saturation experiments (labeled S in Table 2). Bulk composition color codes: synHP1 = dark green, ($n$ = 1); synHP1 + Cr + Mn = light green; HAB + Ol + Mn = dark blue; synMORB80 = purple; synMORB60 = red; synMORB40 = light blue. Triangles – 1175 °C; Circles – 1225 °C; Squares – 1300 °C; Diamonds – 1350 °C; Star – 1400 °C. 1σ errors are smaller than the symbol sizes

the furnace tube (see Supplementary Section S2 and Matzen et al. 2011).

Fo contents (Fo = 100[Mg/(Mg + Fe)], molar) of the experimentally produced olivines range from 57.7 to 92.3 (Fig. 2; the minimum value is from experiment RKD-24, synMORB40 at IW + 0.5 and 1175 °C; the maximum value

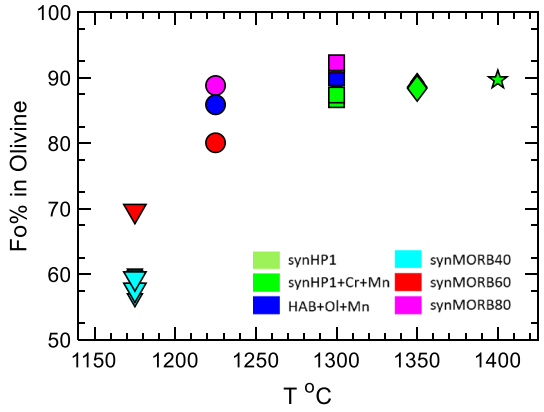


**Fig. 2** Average Fo% (100[Mg/(Mg + Fe)], molar) in olivine rims vs. run T (°C). Symbols as in Fig. 1. 1σ errors are smaller than the symbol sizes

is from experiment RKD-30, synMORB80 at IW–0.5 and 1300 °C). Olivine MnO contents range from 0.14 to 0.74 wt%, and have $Cr_2O_3$ and NiO contents up to 0.50 wt% and 0.73 wt%, respectively (Table 3). All the olivine crystals in experiments conducted at T ≥ 1225 °C have core and rim Fo contents that are indistinguishable within 1σ error (the analytical precision in Fo content ranges from ~ 0.1 for the more magnesian compositions to ~ 0.3 for synMORB40 olivines). However, in the IW–0.5 and IW + 0.5 experiments on the synMORB40 bulk composition run at T = 1175 °C, high-contrast backscattered electron (BSE) images revealed two olivine populations: olivines that were unzoned based on the BSE images, and olivines with cores that were darker than their rims in BSE (Fig. 3). Based on counting visibly zoned grains in the field of view of BSE images, the zoned olivines comprise less than 2% of the olivine grains exposed on the polished chips from each synMORB40 experiment. Microprobe traverses of the zoned olivines show that the cores are approximately 5–6 Fo units more magnesian than the rims; these grains are also zoned in MnO and CaO (this zoning is discussed in Supplementary Section S1.5 and shown in Supplementary Figure S3). However, it is important to stress that in each 1175 °C synMORB40 equilibration experiment, the rim Fo contents of zoned olivines are indistinguishable from the rim compositions of unzoned olivines and it is the rim compositions of unzoned olivines which were used to calculate equilibrium $K_{D,Fe^*\text{-}Mg}$ values (see Table 3 and Fig. 4). Microprobe traverses across olivine grains identified as unzoned in BSE show, with the exception of CaO, no core-to-rim gradients; CaO is elevated in analyses close to the surrounding glass, likely due to secondary fluorescence (Llovet and Salvat 2017). Since we have not corrected rim compositions for Ca fluorescence in any of the experiments, these data should not be used to evaluate olivine–liquid calcium partitioning. In summary, the Fe/Mg

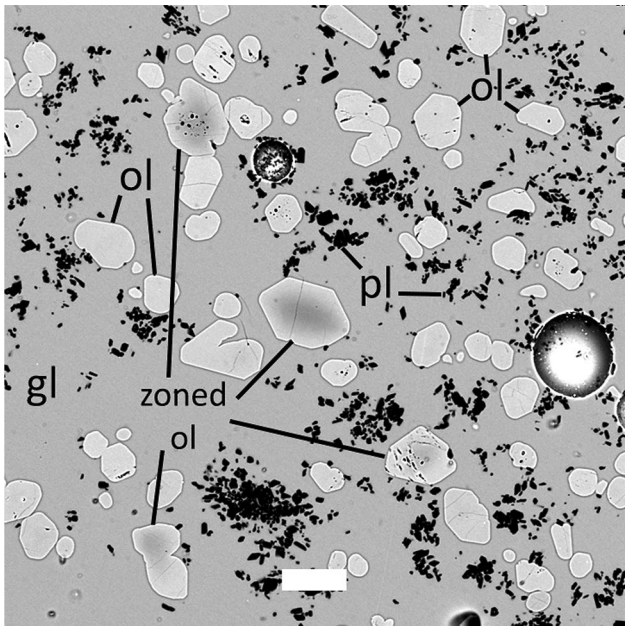


**Fig. 3** Backscattered electron (BSE) image of experimental run products from experiment RKD-22 (synMORB40) with contrast increased to enhance the grayscale zoning in some olivine phenocrysts (labeled "zoned ol"). Scale bar is 40 µm. Phase labels: ol – olivine, gl – glass, pl – plagioclase. Note that most of the olivines in the field of view are unzoned—this area was selected for imaging because it had several zoned olivines visible in the field of view, but they only constitute < 2% of the olivines exposed on the polished chip from the experiment (see Glass and olivine and Supplementary Section S1.5). In the zoned olivines, the cores are ~ $Fo_{67}$ and the rims are ~ $Fo_{60}$; rim compositions of the zoned and unzoned olivines overlap within 1σ

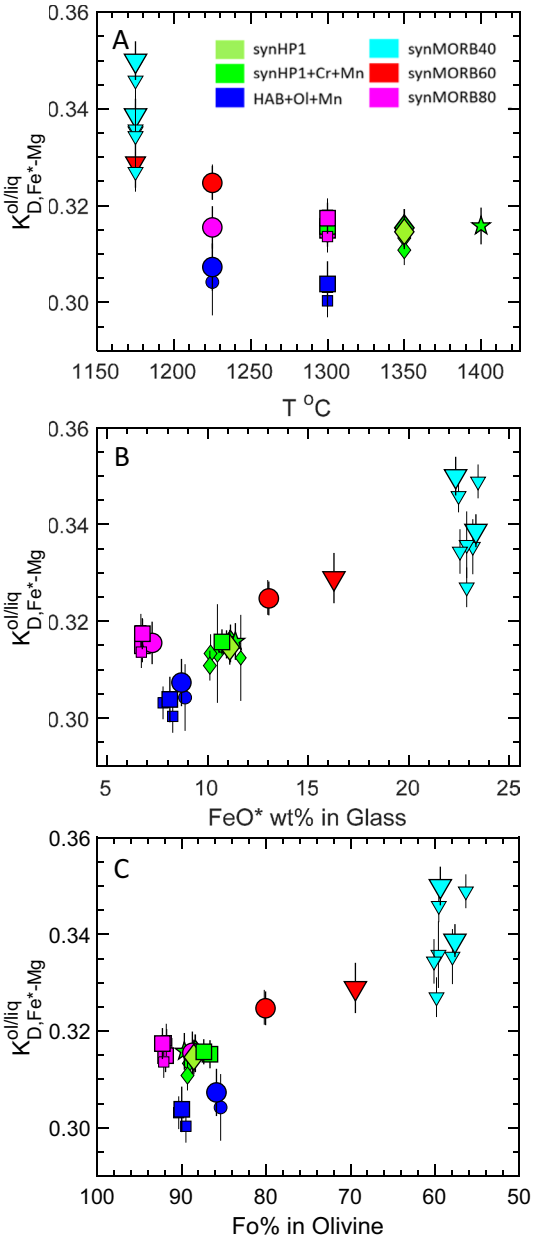


**Fig. 4** Experimentally determined $K_{D,Fe^*-Mg}^{ol/liq}$ ($K_D$*) for RKD experiments run at $fO_2 \leq IW + 0.5$ plotted vs. **A** Temperature, **B** FeO* wt% in glass, **C** Fo% = 100(Mg/[Mg + Fe], molar) in olivine. Symbols as in Fig. 1. The olivine compositions used to calculate $K_{D,Fe^*-Mg}^{ol/liq}$ all come from analyses of olivine rims. Error bars are 1σ and errors for the quantities plotted on the x-axis are smaller than the symbol sizes

ratios of all analyzed olivine rims from a given experiment overlap within analytical uncertainty, and it is the averages of these analyses that are reported in Table 3. We also emphasize that the only equilibration experiments where any Fe/Mg zoning in olivines was observed, either in BSE images or by comparing core and rim analyses, were in the two synMORB40 experiments run at 1175 °C (RKD-24 and RKD-35; for additional details on these two experiments, see Supplementary Section S1.5). We infer that the remaining equilibration experiments approached bulk Fe/Mg equilibrium and were populated entirely by unzoned olivines (note that this includes the 1175 °C experiment on synMORB60).

## Fe–Pt metal blebs

In 19 out of 31 experiments, trace amounts of an Fe–Pt ± Ni metal alloy were observed as isolated blebs in the polished charges (Supplementary Figure S4A and S4B), despite the fact that nominally there was no Pt in any experiments and none of the starting materials made from oxide mixes contained NiO (yet some experiments on these mixes contain Ni-bearing metallic blebs). The proportion of blebs in the experiments is difficult to estimate given their low abundances, but we estimate that they comprise << 0.1% of the experimental volume (see Supplementary Section S1.4). Normalized to 100 wt%, Pt and Fe comprise ≥ 98.4% of the average bleb compositions, and for a majority of the averages, this sum is > 99 wt%. Ni, when present, comprises between ~ 0.09 and 1.6 wt% (detection limit ~ 0.06 wt%) of the average alloy compositions. There are no qualitative

correlations between the presence or absence of the Fe–Pt blebs and Fe loss or gain calculated via mass balance (see Approach to equilibrium and Supplementary Section S3). More details on the blebs and their compositions can be found in Supplementary Section S1.4 and Supplementary Table S1. We speculate that these blebs are produced by contamination from the Pt quench legs from which the Re loops hung, and we note that we have found no evidence that they have measurable effects on the liquid compositions or partitioning results.

## Secondary glass and olivine standards

Analyses of the secondary glass standards (BIR-1g, BHVO-2g, and GOR-128g) constrain the precision and accuracy of the analyses of the experimental glasses. Importantly, for the analytical session in which the RKD glasses were analyzed, the average Fe*/Mg ratio of each secondary glass standard overlaps at 1σ with the global mean Fe*/Mg value for that standard from other sessions in which it was analyzed. The mean and 1σ values of the Fe*/Mg molar ratios measured in the three glasses from the RKD probe session are 0.612 ± 0.005 (BIR-1g, $n = 69$), 0.877 ± 0.009 (BHVO-2g, $n = 73$), and 0.219 ± 0.002 (GOR-128g, $n = 69$). The mean Fe*/Mg values for BIR-1g and BHVO-2g overlap within 1σ of the preferred values for these two glasses listed in the GeoRem database (http:// http://georem.mpch-mainz.gwdg.de; Jochum et al. 2006): 0.621 ± 0.006 (BIR-1g), 0.889 ± 0.008 (BHVO-2g). The Fe*/Mg ratio for GOR-128g overlaps within 2σ of the GeoRem preferred value for GOR-128g (0.212 ± 0.004). Based on data compiled in the GeoRem database, there appear to be relatively small but consistent differences between bulk rock FeO* and MgO values for BIR-1 and BHVO-2 (largely determined by XRF) and the preferred values for BIR-1g and BHVO-2g (determined by electron microprobe). Until this issue is resolved and given the fact that our probe Fe*/Mg values for these standard glasses overlap with the GeoRem preferred values, we have chosen to forego any post-analysis corrections to the glass compositions such as those described in Sack et al. (1980), Reynolds and Langmuir (1997), Stolper et al. (2004), and Gale et al. (2013).

Multiple analyses of nominally homogeneous secondary olivine standards CIT–SC and CIT–GI were used to assess the precision of the analyses of the experimentally produced olivines. In addition to measuring these standards during the same sessions in which the experimental olivines were analyzed, the same standard olivines were measured over several other sessions using different analytical protocols (e.g., counting times, spectrometer choices) and beam conditions. We found no drift at the 1σ level in the Fo contents of the secondary standards within individual sessions or between the sessions in which the RKD experiments were analyzed. Both secondary standards define a narrow range in the Fe/Mg contents calculated from repeat measurements in the analytical sessions where equilibration experiments were measured: CIT–SC, Fo = 89.89 ± 0.05 ($n = 85$) and CIT–GI, Fo = 89.95 ± 0.05 ($n = 90$). Note that published analyses of San Carlos olivines (Jarosewich et al. 1979; Houlier et al. 1990; Spandler and O'Neill 2010; Batanova et al. 2015; Tollan et al. 2018; Lambart et al. 2022) range from Fo = 88.4–91.5, with a mean of 90.5; repeat measurements of the same chip in the CIT–SC olivine mount are slightly more Fe-rich than the mean value above, but are well within the reported range.

## Approach to equilibrium

Several lines of evidence suggest that our experimental results represent close approaches to Fe/Mg equilibrium: for example, (1) olivine and glass are homogeneous within the spatial resolution and analytical precision of the probe analyses (except for the zoned olivine subpopulation in the synMORB40 experiments); (2) time-series experiments converge to a constant value of the FeO*–MgO exchange coefficient; and (3) the overlap between the compositions of the rims of the rare normally zoned olivine grains in the synMORB40 runs and the cores and rims of homogeneous olivine grains in the same experiments suggests progressive conversion of initially more Mg-rich olivine to more Fe-rich olivine with time in the experiments. Further discussion of these three criteria for a close approach to equilibrium is given in Supplementary Section S2.

The proportions of phases in each experiment and estimates of the extent to which FeO*, $Na_2O$, and $K_2O$ were gained or lost during each experiment was determined by mass-balance using a non-linear minimization routine based on Albarède and Provost (1977) (see Supplementary Section S3 for details and Supplementary Table S2 for results). All of the RKD experiments could be mass balanced, yielding acceptable fits at the 95% confidence level. The equilibration experiments run on pre-saturated Re loops lost ≤ 8.3% (relative) of their total FeO* and the average relative change in bulk FeO* was −3.5%. Only one experiment (a saturation run, RKD-22) was found to have gained iron (ΔFeO* = + 1.4% relative). Experiments using the same bulk composition run under identical conditions but with different degrees of FeO* loss have $K_{D,Fe^*-Mg}$ values that overlap at the 1σ level (within 0.003, e.g., compare S and E experiments in Table 2). For the 19 experiments where Fe–Pt blebs were observed, ΔFeO* ranges from < 1% (essentially no change) to –13.4% (in a saturation run), with an average ΔFeO* of –2.9% and is uncorrelated with $X_{Fe}$ in the blebs. The calculated FeO* loss or gain for each experiment is listed in Table 2. Experiments using the alkali-bearing mix HAB + Ol + Mn lost up to 52% of the original $Na_2O$ present

in the bulk mixture, and the two equilibration experiments (RKD-12 and RKD-20) lost approximately 36% and 40% of their initial $Na_2O$, respectively (Supplementary Figure S6 and Supplementary Table S2). The $K_D$* values for all of the HAB + Ol + Mn experiments (run at 1225 °C and 1300 °C and with $Na_2O$ contents from 1.00 wt% to 1.56) overlap at the 1σ level.

### Olivine–liquid partitioning

We proceed by defining the apparent Fe*–Mg exchange coefficient, $K_D$* for an olivine–liquid pair:

$$K^{ol/liq}_{D,\,FeO^*-MgO} = \left(\frac{w_{MgO}}{w_{FeO^*}}\right)^{liq}\left(\frac{w_{FeO}}{w_{MgO}}\right)^{ol} \equiv K_D^* \quad (2)$$

where $w_{MgO}$, $w_{FeO}$, and $w_{FeO^*}$ are the weight percent of MgO and FeO in each phase; as discussed above, all Fe is assumed to be FeO in the olivine and FeO* refers to all Fe as FeO in the liquid. $K_D$* is the shorthand used hereafter and corresponds to the quantity that can be routinely measured using the electron microprobe, where all Fe present in the glass is expressed as FeO. Because $FeO^{liq}$ is always less than $FeO^{*liq}$ (e.g., Bowen and Schairer 1935), $K_{D,Fe^{2+}-Mg}$ will always be greater than $K_D$*, and the magnitude of the difference will depend on the $Fe^{3+}/Fe^{2+}$ of the melt. Based on the available parameterizations of $Fe^{3+}/Fe^{2+}$ vs. $fO_2$, T, and liquid composition, the amount of $Fe^{3+}$ in glasses from our experiments at IW + 0.5 is expected to be sufficiently low such that $K_D$* and $K_{D,Fe^{2+}-Mg}$ will generally differ by less than 0.010. The $Fe^{3+}/Fe^{2+}$ models of Nikolaev et al. (1996) and Jayasuriya et al. (2004) lead to slightly larger maximum differences in [$K_{D,Fe^{2+}-Mg}$ − $K_D$*] at IW + 0.5 of 0.022 and 0.019, respectively. Values of $K_D$* and their associated 1σ values (calculated by summing the FeO and MgO fractional errors for olivine and the FeO* and MgO fractional errors for liquid in quadrature) for the RKD experiments are listed in Table 2.

All bulk compositions except for synMORB40 were run at two or more temperatures that spanned a maximum interval of 100 °C (synMORB40 was only run at 1175 °C). The $K_D$* values for experiments using the same bulk composition but run at different temperatures all overlap within 1σ error (Fig. 4A). Thus, based on our experiments, at constant bulk composition and under reducing conditions, temperature changes of ≤ 100 °C do not produce changes in $K_D$* larger than our analytical uncertainty (typical 1σ ≈ 0.003, absolute). However, there are statistically significant differences in $K_D$* between experiments run using different bulk compositions. For example, the HAB + Ol + Mn experiments (dark blue symbols, Fig. 4A) have a uniformly lower mean $K_D$* value than the MORB or picritic bulk compositions run at the same T. The MORB suite of bulk compositions was designed to vary the molar Fe*/Mg ratio while keeping the relative molar proportions of the other oxides approximately constant, and the $K_D$* values for the MORB suite are positively correlated with liquid FeO* (Fig. 4B), consistent with previous studies with liquid FeO* + MgO < 30 wt% (e.g., Longhi et al. 1978; Jones 1988; Kushiro and Walter 1998; Filiberto and Dasgupta 2011). A linear fit weighted by the errors in $K_D$* to the synMORB experiments run at IW + 0.5 ($r^2 = 0.90$) indicates that $K_D$* increases by ~ 0.01 for every 6 wt% increase in liquid FeO*. Likewise, $K_D$* is systematically higher in the experiments with more Fe-rich olivines (Fig. 4C, note the x-axis shows decreasing Fo), reflecting the trend in FeO* in the glass and the observation that higher bulk Fe leads to higher $K_D$*.

The HAB + Ol + Mn, synHP1, and synHP1 + Cr + Mn experiments run at IW + 0.5 are displaced to lower $K_D$* values relative to the trend defined by the MORB suite. The HAB glasses from equilibration experiments have significantly more $Na_2O$ (~ 1.35 wt%) than the other liquid compositions (< 0.5 wt% $Na_2O$), and the synHP1 ± Cr + Mn glasses contain higher $TiO_2$ contents (~ 2 wt%) than the other glasses (with the exception of RKD-21, synMORB60 run at 1175 °C with 2 wt% $TiO_2$). It is well known that increasing the concentrations of either of these two oxides results in a decrease in $K_{D,Fe^{2+}-Mg}$ (e.g., Longhi et al. 1978; Grove and Beaty 1980; Delano 1980; Gee and Sack 1988; Jones 1988; Shi 1993; Xirouchakis et al. 2001), and our $K_D$* results are consistent with these expected trends. Although our bulk compositions have up to ~ 0.8 wt% MnO (compared to typical basaltic values of ~ 0.1–0.2 wt%; e.g., Le Maitre 1976; Gale et al. 2013), our experimental results suggest that such elevated MnO contents have minimal effect on $K_D$*; e.g., RKD-25 (synHP1; 0.18 wt% MnO) and RKD-5 (synHP1 + Cr + Mn; 0.81 wt% MnO), run at the same T and $fO_2$, have indistinguishable $K_D$* values: 0.315 ± 0.004 and 0.315 ± 0.006.

## Discussion

Using the RKD experiments, we develop a quantitative thermodynamic treatment of the compositional effects on $K_{D,Fe^{2+}-Mg}$ described in the previous section, and then expand this treatment by combining our data with a large set of literature experiments with olivine–liquid pairs run at comparably reduced conditions.

### Parameterizing the compositional dependence of $K^{ol/liq}_{D,Fe^{2+}-Mg}$ using the RKD data

Here we briefly introduce the theoretical framework and equations that describe $Fe^{2+}$–Mg equilibrium between olivine and melt. The exchange reaction can be written as:

$$FeO^{liq} + MgSi_{1/2}O_2^{ol} \rightleftarrows FeSi_{1/2}O_2^{ol} + MgO^{liq}, \quad (3)$$

which has an equilibrium constant, $K_3$:

$$K_3 = \left(\frac{a_{MgO}}{a_{FeO}}\right)^{liq}\left(\frac{a_{FeSi_{1/2}O_2}}{a_{MgSi_{1/2}O_2}}\right)^{ol}, \quad (4)$$

where $a_i^{\Phi}$ is the activity of component i in phase $\Phi$. Combining Eq. (4) with Eq. (1) and using the definition $a_i^{\Phi} = X_i^{\Phi}\gamma_i^{\Phi}$, where $X_i^{\Phi}$ and $\gamma_i^{\Phi}$ refer to the mole fraction and activity coefficient of component i in phase $\Phi$, Eq. (4) can be re-written as:

$$K_3 = \left(\frac{X_{MgO}}{X_{FeO}}\right)^{liq}\left(\frac{X_{FeO}}{X_{MgO}}\right)^{ol}\left[\left(\frac{\gamma_{MgO}}{\gamma_{FeO}}\right)^{liq}\left(\frac{\gamma_{FeO}}{\gamma_{MgO}}\right)^{ol}\right] \quad (5)$$

In the special case where the activity coefficients all equal one, or if the product of the $\gamma$ ratios of both phases equals one [i.e., the term in brackets in Eq. (5)], then $K_{D,Fe^{2+}-Mg}^{ol/liq}$ as defined in Eq. (1) is equal to the equilibrium constant, $K_3$. Because Fe* and Mg can routinely be measured precisely in both olivine and liquid (and, as emphasized above, for experiments at ~ IW the correction for $Fe^{3+}$ in the liquid is small), the unknown parameters in Eq. (5) are the activity coefficients in each phase, which are functions of composition, T, and P. It has long been recognized that using exchange reactions to model mineral-melt equilibria is useful, because the temperature dependence of the ratio of partition coefficients (i.e., $D_i^{ol/liq} = \frac{X_i^{ol}}{X_i^{liq}}$, and $\frac{D_{Fe^{2+}}^{ol/liq}}{D_{Mg}^{ol/liq}} = K_{D,Fe^{2+}-Mg}^{ol/liq}$) is significantly smaller than that of each individual partition coefficient (e.g., Roeder and Emslie 1970; Longhi et al. 1978; Ford et al. 1983; Matzen et al. 2011). In the case of Fe–Mg olivine, this is a consequence mainly of the small differences in the enthalpies of fusion of fayalite and forsterite (Toplis 2005). Therefore, it is often assumed that the effect of temperature on the $K_{D,Fe^{2+}-Mg}$ can be ignored (e.g., Blundy et al. 2020), except through the indirect influence of T on activity-composition relations in the olivine and liquid (e.g., Ghiorso et al. 1983). The pressure dependence of $K_{D,Fe^{2+}-Mg}$ largely reflects the differences in the volumes of fusion of the olivine end members, and on this basis, the pressure effect on the $K_{D,Fe^{2+}-Mg}$ is predicted to be small (on the order of 0.008 absolute per 10 kbar, Ulmer 1989; Herzberg and O'Hara 1998; Toplis 2005). Based on this small effect, we have not included a pressure term in our expression for $K_{D,Fe^{2+}-Mg}$, because the pressures in our combined data set discussed below (our experiments and those from the literature) only range from 1 to 260 bars (nevertheless, adding a pressure term would be straightforward, e.g., Eq. (9) in Toplis 2005).

To parameterize the compositional dependence of $K_{D,Fe^{2+}-Mg}$, we have adopted the general approach of Toplis (2005), specifically, their Eq. (5):

$$\ln K_{D,Fe^{2+}-Mg}^{ol/liq} = \frac{\Delta G^{\circ}}{RT} + \ln\left(\frac{\gamma_{FeO}}{\gamma_{MgO}}\right)^{liq} + \frac{W_{Fe-Mg}^{ol}}{RT}\left(1 - 2\,X_{Fo}^{ol}\right) \quad (6)$$

where $W_{Fe-Mg}^{ol}$ is an interaction parameter describing Fe–Mg non-ideality in a symmetric binary olivine solid solution and $\Delta G^{\circ}$ is the standard state Gibbs free energy change of reaction (3). Equation (6) explicitly takes into account non-ideality in both the olivine and the liquid. Toplis (2005) inferred that the ratio $(\frac{\gamma_{FeO}}{\gamma_{MgO}})^{liq}$ is a function of the $SiO_2$ and alkali contents of the liquid and constructed empirical functions that describe that relationship (see Appendix 2 in Toplis 2005). We have adopted a functional form for the activity coefficients in the liquid based on a truncated symmetric, strictly regular solution model (e.g., Ghiorso 1983) excluding, for now, any cross-terms in the Margules parameters (i.e., all of the W interaction terms are symmetric and each pair of binary interaction terms is independent of the others and of temperature):

$$RT\ln\gamma_i^{liq} = \sum_j W_{i-j}^{liq} X_j^{liq};\ j \neq i \quad (7)$$

where $i$ = MgO or FeO, $W_{i-j}^{liq}$ is the binary interaction parameter, $X_j^{liq}$ is the single-cation mole fraction of component j in the liquid, and $j \neq i$ indicates that there are no terms for MgO–MgO or FeO–FeO in the summation. Because only the ratio $(\frac{\gamma_{FeO}}{\gamma_{MgO}})^{liq}$ is considered, Eq. (6) can be simplified by taking the difference of the expressions for i = FeO and MgO, and defining $B_j \equiv [W_{FeO-j}^{liq} - W_{MgO-j}^{liq}]$, giving:

$$RT\ln\left(\frac{\gamma_{FeO}}{\gamma_{MgO}}\right)^{liq} = \sum_j B_j X_j^{liq} \quad (8)$$

Note that because the formulation is a symmetric solution, FeO–MgO and MgO–FeO terms would be equivalent and thus would cancel when expressed in terms of the $B_{FeO-MgO}$ parameter. Equation (8) can be substituted into Eq. (6) to give the following thermodynamically based equation, where the $B_j$ terms are adjustable parameters that describe the ratio of the compositional dependences of the MgO and FeO activity coefficients in the liquid as a result of interactions with other liquid components (e.g., $SiO_2$, alkalis, etc.), and where $W_{Fe-Mg}^{ol}$ is an adjustable parameter for non-ideality in the olivine. Following the discussion in Jayasuriya et al. (2004), we explored using either $B_jX_j/RT$

or $B_jX_j$ terms in Eq. (6). Preliminary fits to the RKD data and the literature data (discussed in the next section) had smaller average absolute deviations when we used $B_jX_j$ terms. Thus, Eq. (6) becomes:

$$\ln K_{D,Fe^{2+}-Mg}^{ol/liq} = \frac{\Delta G^\circ}{RT} + \sum_j B_j X_j^{liq} + \frac{W_{Fe-Mg}^{ol}}{RT}\left(1 - 2X_{Fo}^{ol}\right) \quad (9)$$

The expression for $\Delta G^\circ$ in Eq. (9) ($\Delta G^\circ = -6766 - 7.34\ T(K)$, J/mol) is taken directly from Toplis (2005).

As discussed above, another consideration in fitting the compositional dependence of $K_{D,Fe^{2+}-Mg}$ is that routine microprobe measurements of Fe are reported as FeO*, but the exchange coefficient is based on the FeO contents of the liquids—which are generally unknown but can be calculated. Although the low $fO_2$ of the RKD experiments minimized $Fe^{3+}/Fe^{2+}$, $Fe^{3+}$ will still be present even in silicate melts that reach metal saturation (e.g., Bowen and Schairer 1935). Using nine of the available expressions for $Fe^{3+}/Fe^{2+}$ in silicate liquids (Sack et al. 1980; Kilinc et al. 1983; Borisov and Shapkin 1989; Kress and Carmichael 1991; Nikolaev et al. 1996; Jayasuriya et al. 2004; Putirka 2016; Borisov et al. 2018; O'Neill 2018, with the correction from Berry and O'Neill 2022), the maximum $Fe^{3+}/Fe^*$ (i.e., $Fe^{3+}/[Fe^{3+} + Fe^{2+}]$, molar) values calculated in the IW + 0.5 experimental liquids range from 0.02 (O'Neill 2018) to 0.06 (Nikolaev et al. 1996); the median $Fe^{3+}/Fe^*$ value for all the IW + 0.5 experiments using all of the models is 0.03. For the IW + 0.5 experiments, using the minimum estimate of $Fe^{3+}/Fe^* = 0.02$ in the liquid results in a correction, [$K_{D,Fe^{2+}-Mg} - K_D^*$], of ~ 0.006 absolute, which is comparable to our 2σ measurement error; the correction for a liquid with $Fe^{3+}/Fe^* = 0.03$ is ~ 0.010 absolute. For those experiments run at IW–0.5 the maximum estimated $Fe^{3+}/Fe^*$ ranges from 0.01 (O'Neill 2018) to 0.04 (Nikolaev et al. 1996) with a median of 0.02, consistent with estimates of 1.5–2.6% $Fe^{3+}$ in Fe-saturated systems (Bowen and Schairer 1935) and implies that corrections for these more reducing experiments would be within the analytical uncertainty. Importantly, for any of the individual parameterizations, the variation in calculated $Fe^{3+}/Fe^*$ for experiments with different bulk (and thus, melt) compositions equilibrated at the same T and $fO_2$ is less than 0.01 absolute; a difference of 0.01 in $Fe^{3+}/Fe^{2+}$ translates to a [$K_{D,Fe^{2+}-Mg} - K_D^*$] value of ~ 0.003, which is $\lessapprox$ the 1σ analytical uncertainty on $K_D^*$. Thus, based on the nine $Fe^{3+}/Fe^{2+}$ models that we have considered, we conclude that any variations in $K_D^*$ in our experiments run at the same T and $fO_2$ that are larger than the analytical uncertainties, as well as the overall range in $K_D^*$ of ~ 0.05 absolute observed in the RKD experiments (Fig. 4), must reflect the effects of liquid composition on $K_{D,Fe^{2+}-Mg}$ and not the effects of liquid composition and T on the $Fe^{3+}/Fe^{2+}$ ratio.

Equation (9) was fit to the 14 RKD equilibration experiments listed in Table 2. Although, as described in the previous paragraph, at $fO_2 \leq IW + 0.5$ liquid $Fe^{3+}/Fe^{2+}$ contents are low, we have nevertheless chosen to make the small correction to $K_D^*$ and fit $K_{D,Fe^{2+}-Mg}$. Based on the analysis of Blundy et al. (2020) and Cottrell et al. (2022), we chose the Borisov et al. (2018) model to calculate liquid $Fe^{3+}/Fe^{2+}$. A weighted linear least-squares routine was used to calculate the best-fit values of the unknown coefficients in Eq. (9). Errors on $FeO^{liq}$ were taken from those on $FeO^{*liq}$ and scaled with the calculated ratio $(FeO/FeO^*)^{liq}$ from Borisov et al., i.e., uncertainties associated with the Borisov et al. (2018) coefficients were not considered.

Different combinations of $X_j^{liq}$ in the $\sum_j B_j X_j^{liq}$ summation (Eq. 9) were tested to find the minimum number of liquid compositional terms required to explain the variability in our experimental $K_{D,Fe^{2+}-Mg}$ values, subject to the constraint that all coefficients satisfy a *t* test at the 95% confidence level. This exercise showed that, in addition to the $W_{Fe-Mg}^{ol}$ term, only one liquid compositional variable, $X_{Si}^{liq}$, was required to fit the RKD experimental data. Si is a critical component of melt structure (e.g., Hess 1971; Mysen et al. 1982; Mysen 1990; Mills et al. 2012) and it has been an important component in several previous parameterizations of $K_{D,Fe^{2+}-Mg}$ (e.g., Longhi et al. 1978; Gee and Sack 1988; Toplis 2005; Putirka 2016). This exercise confirms the conclusion of Toplis (2005) that $SiO_2$ is correlated with $(\frac{\gamma_{FeO}}{\gamma_{MgO}})^{liq}$ (see their Fig. 5). Note that this fitting exercise does not preclude that other interaction terms (and cross-terms) in the liquid are non-zero (which they surely must be), only that including them does not improve the quality of the fit to our experimental $K_{D,Fe^{2+}-Mg}$ values, which are based on liquids that have a small range of alkali and $TiO_2$ contents. Below, we return to the effects of other liquid components on $K_{D,Fe^{2+}-Mg}$.

Figure 5A compares the measured and calculated $K_{D,Fe^{2+}-Mg}$ values for the RKD experiments given the best-fit parameters ($B_{Si} = 1.0259 \pm 0.0213$ and $W_{Fe-Mg}^{ol} = 3291 \pm 182$, where the uncertainties are based on applying weights to the linear regression using the 1σ errors on $K_{D,Fe^{2+}-Mg}$ calculated for each experiment). This result, referred to as Model 1, yields an average absolute deviation (a.a.d.) between the measured and predicted $K_{D,Fe^{2+}-Mg}$ values of 0.0026, which is the same as the typical 1σ analytical precision in $K_{D,Fe^{2+}-Mg}$ ($\pm 0.003$). The best-fit value for $W_{Fe-Mg}^{ol}$ ($3291 \pm 182$) overlaps previous literature estimates ($3700 \pm 800$ J/mol, Wiser and Wood 1991; $2600 \pm 500$ J/mol, O'Neill et al. 2003; 3000 J/mol, Toplis 2005; and $3060 \pm 980$ J/mol, Tuff and O'Neill 2010).

It is worth reemphasizing that given the relatively low concentrations and restricted range in $Na_2O + K_2O$ and $TiO_2$

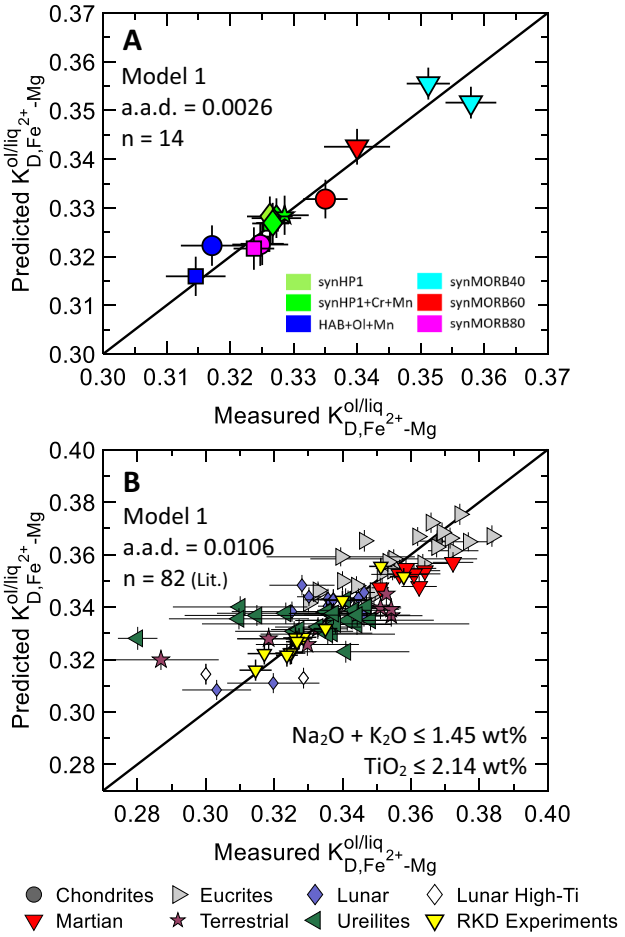


**Fig. 5** Predicted $K^{ol/liq}_{D,Fe^{2+}-Mg}$ using Model 1 (function of T, $X^{liq}_{Si}$, and olivine composition) vs. the experimentally measured values for **A** the RKD experiments ($n=14$), symbols are the same as in Fig. 1, and **B** for a subset of the low-$fO_2$ literature (Lit.) experiments with liquids that contained ≤ 1.45 wt% $Na_2O+K_2O$ and ≤ 2.14 wt% $TiO_2$ ($n=82$) plus the RKD experiments ($n=14$). Alkali and $TiO_2$ bounds are based on the maximum $Na_2O+K_2O$ and $TiO_2$ contents in the RKD glasses. Gray circles – chondrites; gray triangles (right facing) – eucrites; blue diamonds – lunar; white diamonds – lunar high-Ti; red triangles (down-facing) – Martian; maroon stars – terrestrial; green triangles (left-facing) – ureilites; yellow triangles (down-facing) – RKD experiments shown in panel **A**. $Fe^{3+}/Fe^{2+}$ in the glasses was calculated using Borisov et al. (2018) at the T and $fO_2$ of each experiment; a.a.d. is the average absolute deviation in measured $K^{ol/liq}_{D,Fe^{2+}-Mg}$ – predicted $K^{ol/liq}_{D,Fe^{2+}-Mg}$; in panel **B**, a.a.d. reflects only the literature data. The black diagonal line in each panel is a 1:1 line. Error bars are 1σ. Best-fit parameters for Model 1 are listed in Table 4

in the glasses from our equilibration experiments (0.07–1.45 wt% and 0.60–2.14 wt%, respectively), these oxides are not needed to describe the compositional dependence of $K_{D,Fe^{2+}-Mg}$ in the RKD experiments. Including $B_j$ terms for the alkalis and/or Ti does improve the fit, as would be expected by the addition of one or two additional parameters, but the added variables fail a *t* test for significance and thus the improved fit is indistinguishable at the 95% confidence level from the fit, where these $B_j$ values are set to zero. Nevertheless, Model 1 (with $B_{Ti}$ and $B_{Na+K}=0$) overestimates the $K_{D,Fe^{2+}-Mg}$ values for the two HAB + Ol + Mn equilibration experiments by 0.001 to 0.005 absolute (blue symbols in Fig. 5A). As discussed above, these two experiments have alkali contents in the liquid that are higher than the other RKD runs and thus the model misfit, although small, is consistent with the expected effect of alkalis on $K_{D,Fe^{2+}-Mg}$ (e.g., Toplis 2005). To model the effect of alkalis and Ti on $K_{D,Fe^{2+}-Mg}$, in the following discussion we fit Eq. (9) to a data set that includes both our experiments and a compilation of low-pressure olivine-bearing experimental liquids run at $fO_2$ values ≤ IW + 0.5 that span a wide range of $Na_2O+K_2O$ and $TiO_2$ contents.

## Literature data: olivine–liquid experiments at $fO_2 \le$ IW + 0.5

Previous experimental studies at low $fO_2$ have generally focused on lunar, martian, and asteroidal bulk compositions, because most igneous processes on those bodies occur under more reducing conditions compared to those on Earth (e.g., Wadhwa 2008; Putirka 2016). A literature search for nominally anhydrous experiments run at or near atmospheric pressure and at $fO_2 \le$ IW + 0.5 returned 42 studies published between 1975 and 2021 containing 305 individual experiments with quantitative olivine and liquid data. Of these 305 experiments, 276 provided complete compositional information on all silicate and oxide phases, a prerequisite for mass balance, which is one of our tests for evaluating the consistency of the experiments and phase analyses. These 276 experiments can be categorized by provenance and bulk composition, i.e., high- and low-Ti lunar basalts, martian basalts, eucrites, etc.; the complete list and associated references are reported in Supplementary Section S4. The literature data set covers a much broader region of composition space than that sampled by the RKD experiments and includes liquid compositions with up to 18.4 wt% $TiO_2$, 8.4 wt% $Na_2O$, 1.94 wt% $K_2O$, and experimental olivines with Fo contents between 32.6 to 96.2 mol percent. Liquid compositions range from quartz normative (78% of the experiments) to nepheline normative (6%); 94% of the liquids have normative hypersthene and 22% contain normative olivine (CIPW norms calculated with all Fe as FeO). The differentiation index (D.I.; Thornton and Tuttle 1960) of these glasses range from 15 to 88 with a median value of 38, i.e., roughly basaltic in composition.

For each literature experiment, all phase compositions (and uncertainties where provided) were compiled into a database along with the experimental run conditions. The $fO_2$ of experiments run in pure Fe capsules was calculated using the activity model of Snyder and Carmichael (1992)

and using a ΔG° for the reaction Fe + ½ $O_2$ = FeO calculated from the thermodynamic data of Robie et al. (1979), assuming that the activity of Fe in the metal phase was unity. Otherwise, the $fO_2$ values entered into the database are those reported in each study: oxygen sensor measurements; calculated from the buffer along which the experiment was run (e.g., IW); or, for graphite capsules, calculated from C–O equilibria (French and Eugster 1965). These $fO_2$ values were used to calculate liquid FeO and $Fe_2O_3$ values for each of the experimental glasses (using Borisov et al. 2018) and the $FeO^{liq}$ concentrations were then used to calculate the $K_{D,Fe^{2+}-Mg}$ values.

Each of the 276 literature experiments was subjected to the same quality control tests as were applied to the RKD experiments, albeit with slightly more lenient bounds for glass and olivine oxide sums, olivine stoichiometry, and mass balance (details are given at the end of the Supplementary Section S3). Of the 276 experiments that had sufficient compositional information to run the mass balance calculation, 200 (72%) had suitable fits at the 95% confidence level. Experiments that failed mass balance were flagged as potentially problematic and were not included in the fitting exercises. For those experiments that did not crystallize an Fe metal phase and passed mass balance, the mean calculated Fe-loss was −4.0% relative (the median value was –0.7% relative; 14 out of the 200 experiments had Fe-loss greater than −10%, with a maximum loss of −39.1%; and only two experiments gained more than + 5% Fe (maximum gain was + 12.8% relative)). Although such large amounts of Fe loss or gain could lead to olivine–liquid $Fe^{2+}$–Mg disequilibrium, an Fe-loss rejection criterion was not applied to the literature data. Depending on the run temperature and duration and whether the loss occurred early or continuously during an experiment, it is possible that the olivine rim compositions re-equilibrated with the melt, thus making it difficult to choose a cutoff that is not arbitrary. Application of the data quality filters (see Supplementary Section S3) resulted in a preferred data set of 187 experimental olivine–liquid pairs that cover a temperature range of 1050 to 1503 °C and a compositional range that is comparable to that of the full set of 276 experiments.

Before using the preferred literature data set to determine which other liquid compositional terms in the summation in Eq. (9) are significant, we applied Model 1 (which was fit only to the RKD experiments) to the 82 literature experiments with $TiO_2$ and $Na_2O + K_2O$ concentrations less than or equal to the maximum concentrations present in the RKD glasses used to calibrate Model 1 (≤ 2.14 wt% $TiO_2$ and ≤ 1.45 wt% $Na_2O + K_2O$). As discussed above, a large body of experimental data has shown that $K_{D,Fe^{2+}-Mg}$ values correlate with liquid alkalis and $TiO_2$ contents (e.g., Longhi et al. 1978; Grove and Beaty 1980; Delano 1980; Gee and Sack 1988; Jones 1988; Shi 1993; Xirouchakis et al. 2001). Predicted (Model 1) vs. experimental $K_{D,Fe^{2+}-Mg}$ values ($Fe^{2+}$ calculated using Borisov et al. 2018) are shown in Fig. 5B. The average absolute deviation (a.a.d.) between the measured and predicted $K_{D,Fe^{2+}-Mg}$ values for these low-Ti and low-alkali literature experiments is 0.0106, which is substantially higher than the 0.0026 from the RKD experiments (shown in Fig. 5B as yellow triangles). It is important to emphasize that the analytical precision of the literature data is typically worse than that associated with the RKD experiments—only 49 out of the 82 low-alkali and low-$TiO_2$ literature experiments report FeO* and MgO uncertainties in both phases, and for these 49 experiments the mean 1σ for $K_{D,Fe^{2+}-Mg}$ is 0.0105 (compared to 0.0026 for the RKD experiments). Therefore, for both the high-precision RKD data and those literature data with reported compositional errors and similar ranges in $TiO_2$ and $Na_2O + K_2O$, Model 1 recovers $K_{D,Fe^{2+}-Mg}$ values to approximately the reported analytical precision. More specifically, for 42 out of these 49 experiments, the model $K_{D,Fe^{2+}-Mg}$ values overlap their experimental values at 2σ.

## Modeling the compositional dependence of $K^{ol/liq}_{D,Fe^{2+}-Mg}$ using the RKD and literature data sets

In this section we describe a fit that combines both the RKD experiments and the preferred low-$fO_2$ literature data set ($n$ = 201) that, as discussed above, covers a much wider compositional range than the RKD experiments. Based on exploring different combinations of compositional terms, we found that, in addition to terms for Ti and Na + K, an Si-(Na + K) cross-term[1] (i.e., $X_{Si}$ multiplied by the sum $[X_{Na} + X_K]$ in the liquid) was required to describe the non-ideality of FeO and MgO in liquids with high alkali and silica contents ($SiO_2 \gtrapprox 55$ wt% and $Na_2O + K_2O \gtrapprox 4$ wt%). Other liquid compositional terms were tested including a Si–Si interaction term, individual coefficients for Na and K, and cross-terms including Si-Ti and Ti-(Na + K), but only Si-(Na + K) led to a significant improvement in the fits to the measured exchange coefficients ($p < 0.05$ based on comparing the t-statistic for the model fits). The need for an Si-(Na + K) cross-term to fit the high-alkali and high-silica olivine–liquid exchange data is not surprising given the significant effect that alkalis have on the activity of $SiO_2$ in silicate melts (e.g., Kushiro 1975; Watson 1982; Ryerson 1985; Grove and Juster 1989; Hirschmann et al. 1998) and that both alkalis and silica have on the activity of FeO in melts (e.g., O'Neill 2022). When fitting $K_{D,Fe^{2+}-Mg}$ to the literature

[1] Equation (7) can be expanded to include cross-terms: $RT\ln\gamma_i^{liq} = \sum_j W_{i-j}^{liq} X_j^{liq} - \frac{1}{2}\sum_j \sum_k W_{j-k}^{liq} X_j^{liq} X_k^{liq}$ (Ghiorso et al. 1983), where i = MgO or FeO, and in this case j = $SiO_2$, and k = ($NaO_{0.5} + KO_{0.5}$); the W parameters are symmetric (i.e., $W_{i-j} = W_{j-i}$ and $W_{i,j-k} = W_{i,k-j}$). Following Eq. (8) and the definition $B_{j-k} \equiv [W^{liq}_{FeO-[j-k]} - W^{liq}_{MgO-[j-k]}]$, it follows that $B_{Si-(Na+K)} = W_{Si-(Na+K)}$.

**Table 4** Values of fit parameters for $\ln K^{ol/liq}_{D,Fe^{2+}-Mg}$, $\ln D^{ol/liq}_{Mg}$, and $\ln D^{ol/liq}_{Fe^{2+}}$

| | | $B_{Si}$ | $B_{Ti}$ | $B_{Si-(Na+K)}$ | $W^{ol}_{Fe-Mg}$ | ΔG° (Toplis 2005) | $\overline{\Delta K}^{ol/liq}_{D,Fe^{2+}-Mg}$ (Exp-Calc) | $\lvert\Delta K^{ol/liq}_{D,Fe^{2+}-Mg}\rvert$ (a.a.d.) |
|---|---|---|---|---|---|---|---|---|
| Model 1 | | 1.0259 | | | 3291 | –6766 – 7.34 T | –0.0007 | 0.0026 |
| ($n=14$) | 1σ | 0.0213 | | | 182 | | | |
| Model 2 | | 1.0445 | –1.3125 | –3.0550 | 3040 | –6766 – 7.34 T | –0.0016 | 0.0141 |
| ($n=201$) | 1σ | 0.0202 | 0.1076 | 0.1851 | 158 | | | |
| | | $A_i$ | $C_i$ | $F_i$ (Beattie 1993) | SSR | $\overline{\Delta T}$ (Exp-Calc) | \|ΔT\| (a.a.d.) | $\lvert\Delta D^{ol/liq}_i\rvert$ (a.a.d.) |
| $\ln D^{ol/liq}_{Mg}$ | | 13,428 | 6.224 | 0.049 | $1.24\times 10^5$ | +0.02° | 19° | 0.353 |
| ($n=201$) | 1σ | 284 | 0.191 | | | | | |
| $\ln D^{ol/liq}_{Fe2+}$ | | 12,592 | 7.916 | 0.048 | $1.82\times 10^5$ | +0.05° | 23° | 0.147 |
| ($n=201$) | 1σ | 335 | 0.225 | | | | | |

Fitted parameters for the olivine–liquid exchange coefficient, $\ln K^{ol/liq}_{D,Fe^{2+}-Mg} = \frac{\Delta G^\circ}{RT} + \sum_j B_j X^{liq}_j + \frac{W^{ol}_{Fe-Mg}}{RT}\left(1 - 2X^{ol}_{Fo}\right)$, Eq. (9), and for the individual partition coefficients, $\ln D^{ol/liq}_i = 0.5(A_i/T + (P-1)F_i/T - C_i - 2\ln(1.5NM) - 2\ln(3X^{liq}_{Si}) + NF)$, where i = Mg or $Fe^{2+}$, Eqs. (11) and (12); T is in Kelvin and R is in J/(mol K). Model 1 refers to the fit to the RKD experiments only ($n=14$, see Parameterizing the compositional dependence of $K^{ol/liq}_{D,Fe^{2+}-Mg}$ using the RKD data); Model 2 is fit to both the RKD experiments ($n=14$) and the preferred low-$fO_2$ compilation of literature experiments ($n=187$; see Modeling the compositional dependence of $K^{ol/liq}_{D,Fe^{2+}-Mg}$ using the RKD and literature data sets). The ΔG° term was adopted from Toplis (2005) and is not a fitted parameter. $\overline{\Delta K}^{ol/liq}_{D,Fe^{2+}-Mg}$ is the average difference between the experimental and calculated value for $K^{ol/liq}_{D,Fe^{2+}-Mg}$, whereas $\lvert\Delta K^{ol/liq}_{D,Fe^{2+}-Mg}\rvert$ is the average absolute deviation (a.a.d.) between the experimental and calculated values. Uncertainties in Model 1 and Model 2 are based on the 1σ errors in $K^{ol/liq}_{D,Fe^{2+}-Mg}$ used as weights in the fitting procedure and do not include errors for the liquid compositional variables used in the fits. The individual partition coefficients, $\ln D^{ol/liq}_{Mg}$ and $\ln D^{ol/liq}_{Fe^{2+}}$, were fit to the combined low-$fO_2$ compilation ($n=201$) as described in Practical application of the model for $K^{ol/liq}_{D,Fe^{2+}-Mg}$. The values for the $F_i$ pressure term for both the Mg and $Fe^{2+}$ models were taken from Beattie (1993) and were not fitted parameters. $X^{liq}_{Si}$ is the single-cation mole fraction of Si in the liquid, $NM = X^{liq}_{Fe} + X^{liq}_{Mn} + X^{liq}_{Mg} + X^{liq}_{Ca} + X^{liq}_{Ni}$, and $NF = 7/2\ln(1 - X^{liq}_{Al}) + 7\ln(1 - X^{liq}_{Ti})$. SSR is the sum of the squared residuals. ΔT is the average of the differences between the experimental and calculated temperatures in degrees, whereas |ΔT| is the average absolute deviation (a.a.d.) between the experimental and calculated temperatures

data set, it was found that the $B_{Na+K}$ term could be omitted while retaining $B_{Si-(Na+K)}$ without reducing the overall quality of the fit. Thus, the following set of liquid compositional terms were included in Eq. (9): $B_{Si}$, $B_{Ti}$, and $B_{Si-(Na+K)}$.

Given that the literature data set is substantially larger than the RKD data set, we used an iterative approach for fitting the three liquid compositional terms and one olivine compositional term that provides sufficient weight to the much smaller set of RKD experiments:

(1) Best-fit coefficients $B_{Si}$ and $W^{ol}_{Fe-Mg}$ were first determined by fitting the high-precision RKD experimental data to Eq. (9) with $B_{Ti}$, and $B_{Si-(Na+K)}$ set to zero.
(2) With the $B_{Si}$ and $W^{ol}_{Fe-Mg}$ values held constant, a second least-squares fit to Eq. (9) was done using the only literature data ($n=187$) to constrain the values of $B_{Ti}$ and $B_{Si-(Na+K)}$.
(3) Now fixing $B_{Ti}$ and $B_{Si-(Na+K)}$ to the values determined in step (2), the RKD data alone were used to refit the $B_{Si}$ and $W^{ol}_{Fe-Mg}$ coefficients.
(4) Finally the literature data were refit for $B_{Ti}$ and $B_{Si-(Na+K)}$, using the values for $B_{Si}$ and $W^{ol}_{Fe-Mg}$ from step (3). Although this procedure could be repeated if necessary, the coefficients were found to converge after steps 1 through 4.

As was the case with the Model 1 fit, the iterative least-squares fits were weighted by the propagated measurement errors in FeO and MgO in the olivines and glasses (each glass FeO error is based on the FeO* error scaled by the calculated $(FeO/FeO^*)^{liq}$ ratio). Where this information was not available, the 1σ FeO and MgO values in each phase were calculated using the empirical FeO* and MgO fractional error equations described in the literature mass balance routine (Supplementary Section S3), with the 1σ $FeO^{*liq}$ values scaled by $(FeO/FeO^*)^{liq}$.

The best-fit values for the $B_j$ coefficients, where j = Si, Ti, and Si–(Na + K), and the coefficient for the olivine term, $W^{ol}_{Fe-Mg}$, using the iterative procedure described above are referred to as Model 2 and are given in Eq. (10) and in Table 4:

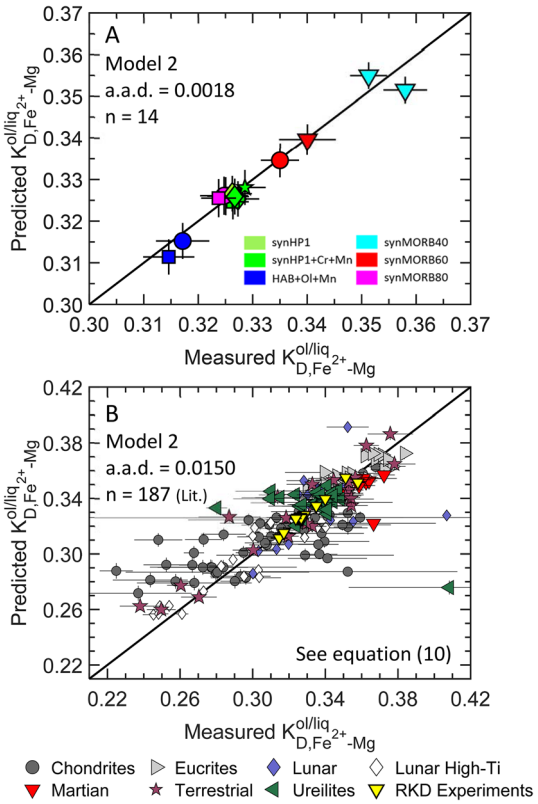


**Fig. 6** Predicted $K_{D,Fe^{2+}-Mg}^{ol/liq}$ values using Model 2 (function of T, $X_{Si}^{liq}$, $X_{Ti}^{liq}$, $X_{Si}^{liq}(X_{Na}^{liq}+X_{K}^{liq})$, and olivine composition) vs. experimentally measured values for **A** the RKD experiments ($n=14$); symbols as in Fig. 1, and **B** for the combined low-$fO_2$ data set ($n=187$ literature (Lit.) experiments plus the $n=14$ RKD experiments); symbols are the same as in Fig. 5B, and are given at the bottom of the figure. For all the experimental glasses, $Fe^{3+}/Fe^{2+}$ was calculated using Borisov et al. (2018) at the T and $fO_2$ of each experiment; a.a.d. is the average absolute deviation in measured $K_{D,Fe^{2+}-Mg}^{ol/liq}$ – predicted $K_{D,Fe^{2+}-Mg}^{ol/liq}$; in panel **B**, a.a.d. reflects only the literature data. The black diagonal line in each panel is a 1:1 line. Error bars are 1σ. Best-fit parameters for Model 2 are listed in Table 4

Both of these values for $W_{Fe-Mg}^{ol}$ overlap at 1σ with the value calculated using just the RKD data (3291 ± 182, Model 1) and all three are within the range of previously reported values (2600–3700 J/mol).

Applying Model 2 to the RKD data set results in an a.a.d. of 0.0018 (Fig. 6A), which is slightly lower than the a.a.d. of 0.0026 calculated using Model 1 (Fig. 5A). Model 2 improves the fit to the HAB + Ol + Mn experiments which have liquid $Na_2O + K_2O \approx 1.4$ wt% (compare blue symbols in Figs. 5A and 6A), consistent with the previously observed effect of lower $K_{D,Fe^{2+}-Mg}$ for liquids with higher alkali contents (e.g., Ford et al. 1983; Gee and Sack 1988; Shi 1993; Toplis 2005; Putirka 2016). For the preferred literature data alone ($n=187$), the a.a.d. is 0.0150 (Fig. 6B); adding those experiments that did not pass mass balance nor the oxide sum and/or stoichiometric constraints ($n=89$) to the preferred data set ($n$ now equal to 276), the a.a.d. is 0.0159. The similarity between the model residuals for the preferred and complete literature data set suggests that the errors in the 89 experiments that did not pass our mass balance and quality filters are approximately normally distributed in composition space. Finally, for the combined low-$fO_2$ data set ($n=201$), the average $\Delta K_{D,Fe^{2+}-Mg}$ value (measured – calculated) is −0.0016 indicating that the distribution is not skewed towards positive nor negative values.

There is no statistically significant correlation between Fe-loss and the Model 2 residuals, suggesting that although a melt may initially lose Fe to the container, the olivine and liquid can then re-equilibrate if the run duration is sufficiently long and/or the temperature is sufficiently high; i.e., under such circumstances $K_D$* could closely approach the equilibrium value despite the experiment not being a perfectly closed system. A failure to closely approach equilibrium, while Fe is being actively lost from the experiment would lead to the interior of the olivine grain having a high Fe/Mg ratio relative to the equilibrium value given the $Fe^{2+}$/Mg ratio in the melt; this in turn would lead to a $K_D$* value higher than the equilibrium value. Crystallization of a metal phase could also produce an elevated $K_D$*, even though the bulk FeO* content of the experimental charge is constant. The opposite effect would be observed if the sample were actively gaining Fe from an Fe capsule, while the olivine cores were shielded by slow diffusion from the rims in contact with the Fe-enriched melt. A lower than expected $K_D$* value would also result if early formed Mg-rich olivines did

$$\begin{aligned}\ln K_{D,Fe^{2+}-Mg}^{ol/liq} &= \frac{\Delta G^{\circ}}{RT} + \sum_{j} B_j X_j^{liq} + \frac{W_{Fe-Mg}^{ol}}{RT}\left(1 - 2X_{Fo}^{ol}\right) \\ &= [-6766 - 7.34T]/RT + 1.0445 \pm 0.0202X_{Si}^{liq} - 1.3125 \pm 0.1076X_{Ti}^{liq} - 3.0550 \pm 0.1851X_{Si}^{liq}(X_{Na}^{liq} + X_{K}^{liq}) \\ &\quad + 3040 \pm 158(1 - 2X_{Fo}^{ol})/RT\end{aligned} \tag{10}$$

where T is in Kelvin, $X_j^{liq}$ is the single-cation mole fraction of element j in the liquid, $X_{Fo}^{ol}$ is the mole fraction of forsterite in olivine, R is the gas constant in J/(mol K), and the values after the ± symbols are 1σ errors. Note that calculating all four parameters using only the literature data results in coefficients that are within error of those shown in Eq. (10), e.g., $W_{Fe-Mg}^{ol}$ calculated using only the literature data is 3044 ± 297 compared to 3040 ± 158 for Model 2.

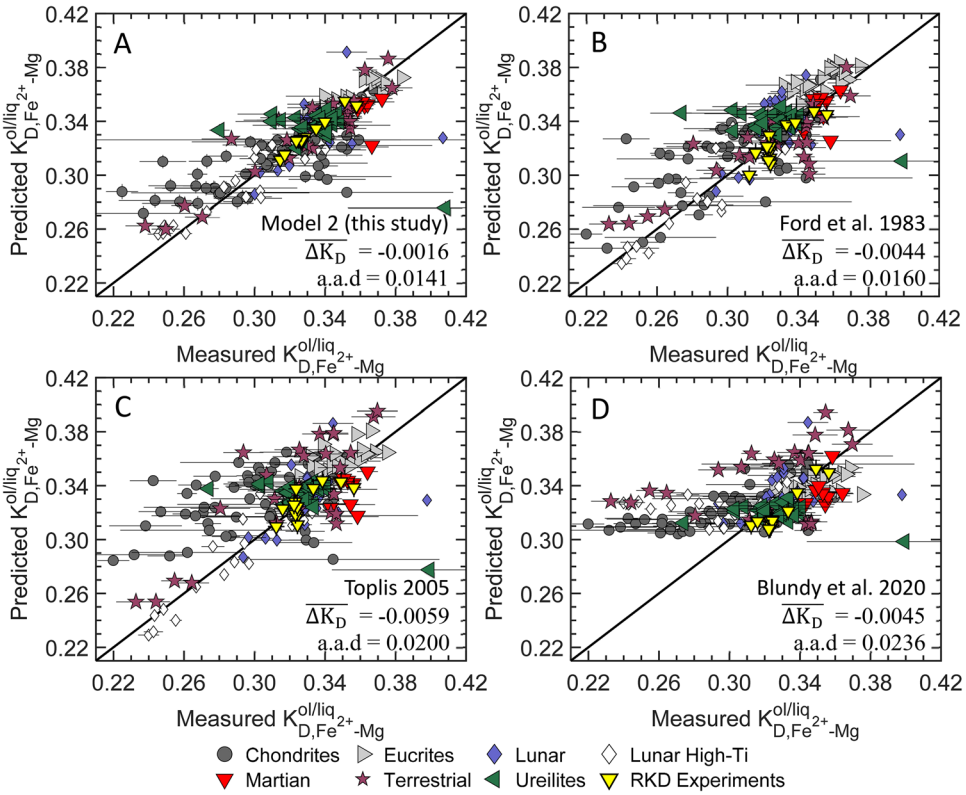


**Fig. 7** Predicted vs. experimentally measured $K^{ol/liq}_{D,Fe^{2+}-Mg}$ values. The data set consists of the RKD experiments ($n = 14$) and the preferred low-$fO_2$ experiments ($n = 187$). **A** Model 2 (this study), **B** Ford et al. (1983), **C** Toplis (2005), **D** Blundy et al. (2020). The expression used to calculate $Fe^{3+}/Fe^{2+}$ for each model is: Borisov et al. (2018), (**A**); Sack et al. 1980, **B**; Kilinc et al. (1983) plus $P_2O_5$ term from Toplis et al. (1994), **C**. Symbols are the same as in Figs. 5B and 6A; a.a.d. refers to the average absolute deviation between the measured value and the value calculated using each model. The diagonal line in each panel is a 1:1 line. Error bars are 1σ

not completely re-equilibrate with melt whose Fe/Mg ratio was increasing due to continued crystallization—note that in this case (as with the case of metal crystallization), the experiment is closed with respect to Fe loss or gain. All of these effects are likely to be more important in lower temperature experiments, where Fe–Mg diffusion in olivine is slower than in higher temperature runs, and indeed the absolute values of the residuals between measured $K_{D,Fe^{2+}-Mg}$ values for the combined RKD and literature data sets and those calculated using Model 2 are inversely correlated with temperature, albeit with considerable scatter. Although the Spearman rank order correlation coefficient is not strong ($r_s = -0.213$), the correlation is significant at greater than the 99% confidence level. Although other explanations are possible—for example, liquids from lower T experiments may share compositional characteristics that are not fully captured by Model 2—the inverse correlation is consistent with the inference that some of the lower temperature literature data did not closely approach bulk olivine–liquid Fe–Mg equilibrium.

## Comparison to previous parameterizations of $K^{ol/liq}_{D,Fe^{2+}-Mg}$

Figure 7A compares $K_{D,Fe^{2+}-Mg}$ values from the composite database of the RKD experiments ($n = 14$) and low-$fO_2$ literature experiments ($n = 187$) with predicted values based on the output of Model 2. Also shown in Fig. 7 are comparisons of the same database of low-$fO_2$ $K_{D,Fe^{2+}-Mg}$ values with predicted values from three other thermodynamically motivated parameterizations of the compositional dependence of $K_{D,Fe^{2+}-Mg}$: Fig. 7B, Ford et al. (1983); Fig. 7C, Toplis (2005); and Fig. 7D, Blundy et al. (2020). In contrast to Model 2, each of these models was calibrated using available data from olivine–liquid experiments run over a wide range of $fO_2$ values extending to oxidizing conditions: (Ford et al. 1983: IW–1 to ~ FMQ + 1.5; Toplis 2005: ~ IW to ~ FMQ + 1.5; Blundy et al. 2020: IW + 1.2 to air[2]). Of the 42 studies used to calibrate Model 2, nine overlap with those used in Ford et al. (1983), three overlap with Toplis (2005), and there is no overlap with the data set used in Blundy et al. (2020) (overlapping studies are listed in Supplementary Section S4).

The Ford et al. (1983) model contains terms for 1/T and P/T, and compositional terms for Mg, $Fe^{2+}$, Ca, Mn, Cr, Ni,

[2] For Ford et al. (1983), the range in $fO_2$ values is based on previously unpublished experimental results of Ford et al. reported in Falloon et al. (2007) and on the papers cited in the reference appendix; For Toplis (2005) and Blundy et al. (2020), the range is based on the experimental literature cited in each work.

Si, Al, $Fe^{3+}$, Na + K, Ti, and P[3] in the liquid and utilizes the Sack et al. (1980) model to calculate $Fe^{3+}/Fe^{2+}$ for each experimental liquid used to calibrate their model. The Toplis (2005) model is the basis of our Eq. (9) and is a function of $X^{ol}_{Fo}$ and $SiO_2$ and $Na_2O + K_2O$ in the liquid; $Fe^{3+}/Fe^{2+}$ was calculated using Kilinc et al. (1983), modified by the $P_2O_5$ term from Toplis et al. (1994). A feature of the Toplis model is that the silica and alkali-based equation used to describe variations in $(\frac{\gamma_{FeO}}{\gamma_{MgO}})^{liq}$ changes from linear to non-linear at 60 mol% silica. The Blundy et al. (2020) model (their Eq. (7)) parameterizes $K_{D,Fe^{2+}-Mg}$ only in terms of olivine composition using 52 experiments, where $Fe^{3+}/Fe^{2+}$ was measured in the coexisting glasses and thus is independent of any $Fe^{3+}/Fe^{2+}$ algorithm. In Fig. 7, $K_{D,Fe^{2+}-Mg}$ values were calculated after first calculating $FeO^{liq}$ using the $Fe^{3+}/Fe^{2+}$ scheme associated with the Ford et al. and Toplis models, respectively.

The average of the measured minus model $K_{D,Fe^{2+}-Mg}$ values ($\overline{\Delta K}_{D,Fe^{2+}-Mg}$) and the a.a.d. values for the four models are: Model 2, $\overline{\Delta K}_{D,Fe^{2+}-Mg} = -0.0016$, a.a.d. = 0.0141; Ford et al. (1983), $\overline{\Delta K}_{D,Fe^{2+}-Mg} = -0.0044$, a.a.d. = 0.0160; Toplis (2005), $\overline{\Delta K}_{D,Fe^{2+}-Mg} = -0.0059$, a.a.d. = 0.0200; and Blundy et al. (2020), $\overline{\Delta K}_{D,Fe^{2+}-Mg} = -0.0045$, a.a.d. = 0.0236. Histograms of the distributions of $\Delta K_{D,Fe^{2+}-Mg}$ for each model are shown in Supplementary Figure S7. Although the mean values of these distributions are all essentially the same, the model of Blundy et al. (2020) does not permit $K_{D,Fe^{2+}-Mg}$ values much less than ~ 0.30, yet such values are a significant fraction (43 out of 201, or 21%) of our low-$fO_2$ data set, especially in experiments that generated high-alkali and high-$TiO_2$ liquids. The low concentrations of $Fe_2O_3$ in all of the experimental liquids in our database makes it difficult to attribute these low $K_{D,Fe^{2+}-Mg}$ values to a compositional dependence of $Fe^{3+}/Fe^{2+}$ that is not captured by the Borisov et al. (2018) model which is used in Model 2. As emphasized by Toplis (2005), the ratio of the FeO and MgO activity coefficients in the melt cannot be treated as a constant except over limited ranges in liquid composition. Thus, liquid compositional terms (such as the $B_j$ coefficients in Eq. (9)) are necessary to describe the effects of variations in liquid composition—especially variations in silica, alkalis, and titania—on $K_{D,Fe^{2+}-Mg}$. We emphasize, however, that it is unclear which, if any, of the functional forms used to describe the liquid solution behaviors is preferable; resolving this issue will likely involve applying independently constrained activity–composition relationships for $FeO^{liq}$ and $MgO^{liq}$ as guides to the proper functional form for the ratio of activity coefficients in Eq. (9).

[3] Note that an error was found in Ford et al. (1983) Table 2 for the reported value of the coefficient on the phosphorus term, $C_{10}\ln(1-P)$: the value for $C_{10}$ should be –3.3034 instead of the reported value of –1.3034.

Model 2 and the Ford et al. (1983) model recover the low-$fO_2$ experimental $K_{D,Fe^{2+}-Mg}$ values with similar degrees of accuracy, but we note that Model 2 uses less than half the number of coefficients of the Ford et al. model. Model 2 and the model of Toplis (2005) differ only in how they parameterize $(\frac{\gamma_{FeO}}{\gamma_{MgO}})^{liq}$, and their overall fits to the data are similar, although the points in Fig. 7C (the Toplis model) have a larger spread in the predicted values and are systematically displaced above the 1:1 line relative the points in Fig. 7A (Model 2). The difference in the parameterization of the activity coefficient ratio does lead, however, to some potentially important differences in the performance of the models. One difference is that the Toplis (2005) model has a change at 60 mol% silica in the functional form used to model $(\frac{\gamma_{FeO}}{\gamma_{MgO}})^{liq}$ and this can lead to a discontinuity in the calculated $K_{D,Fe^{2+}-Mg}$ value: for example, if the $SiO_2$ content of the liquid in run CHS 63 (Collinet and Grove 2020) is increased by ~ 0.25 wt%, the calculated $K_{D,Fe^{2+}-Mg}$ value increases from 0.31 to 0.35.

Both the Ford et al. and the Toplis models were calibrated using 1-atm experimental data sets that covered a much wider range of $fO_2$ than that used to determine the coefficients given in Eq. (10). Thus, for both of these earlier studies, the $Fe^{3+}/Fe^{2+}$ algorithms used to calculate $FeO^{liq}$ exert more leverage on the model coefficients than is the case for this study, where the difference in $FeO^{*liq}$ and calculated $FeO^{liq}$ is small. Since in the comparison above, we are applying the Ford et al. and Toplis models to data that is at the low-$fO_2$ end of their calibration data sets, it is worth considering how well Eq. (10) is able to calculate olivine–liquid $K_{D,Fe^{2+}-Mg}$ values for experiments at higher $fO_2$ (e.g., at FMQ). We used Model 2 to predict $K_{D,Fe^{2+}-Mg}$ values for a database of 454 experimental olivine–liquid pairs run at FMQ ± 0.25 (Matzen et al. 2011); Borisov et al. (2018) was used to calculate $Fe^{3+}/Fe^{2+}$ in the experimental liquids. The average of the $\Delta K_{D,Fe^{2+}-Mg}$ values is + 0.0114, and the a.a.d. is 0.0187. Recall that the corresponding values for the combined low-$fO_2$ calibration data set are $\overline{\Delta K}_{D,Fe^{2+}-Mg} = -0.0016$ and a.a.d. = 0.0141. Thus, applying Eq. (10) to a data set of experiments run at $fO_2$ values three to six log units more oxidizing than those used in the calibration and that have liquids with substantially higher total alkalis (14.3 vs. 8.4 wt%) leads to a small increase in the a.a.d. for the measured vs. modeled $K_{D,Fe^{2+}-Mg}$ values and a small shift towards a positive value for the average of the distribution. For comparison, the Ford et al., Toplis, and Blundy et al. average $\Delta K_{D,Fe^{2+}-Mg}$ and a.a.d. values for the FMQ ± 0.25 data are: $\overline{\Delta K}_{D,Fe^{2+}-Mg} = -0.0007$, a.a.d. = 0.0168; $\overline{\Delta K}_{D,Fe^{2+}-Mg} = +0.0029$, a.a.d. = 0.0149; and $\overline{\Delta K}_{D,Fe^{2+}-Mg} = -0.0103$, a.a.d = 0.0237. We conclude that Eq. (10) can be used to model olivine–liquid $Fe^{2+}$–Mg exchange under conditions much more oxidizing than IW.

Supplementary Section S5 discusses how the different $Fe^{3+}/Fe^{2+}$ models affect experimental $K_{D,Fe^{2+}-Mg}$ values at ≤ IW + 0.5 and FMQ ± 0.25 (also see Supplementary Figures S8 and S9). In the next section, we show how to use Eq. (10) to solve for $K_{D,Fe^{2+}-Mg}$ and Fo given only a liquid composition and $fO_2$ (or $Fe^{3+}/Fe^{2+}$ ratio in the liquid).

## Practical application of the model for $K_{D,Fe^{2+}-Mg}$

One of the practical advantages of a constant $K_{D,Fe^{2+}-Mg}$ (e.g., as assumed by Roeder and Emslie 1970) is that because it is independent of temperature and phase composition, one can simply and directly calculate the equilibrium olivine composition coexisting with a melt (assuming the cation fractions of Mg and Fe in olivine sum to 2/3). Given the olivine and coexisting liquid compositions, one can then calculate the partition coefficient for Mg (i.e., $D_{Mg}^{ol/liq}$), and from the simple linear relationship observed between $lnD_{Mg}^{ol/liq}$ and 1/T (or alternatively, ln $D_{Fe2+}^{ol/liq}$ and 1/T), calculate T (Roeder and Emslie 1970). Application of Eq. (9) is less straightforward, because $K_{D,Fe^{2+}-Mg}$ is no longer a constant, but rather is a function of liquid composition (i.e., the $X_j^{liq}$ s), olivine composition, and T. A simple solution is possible if the liquidus temperature for a given liquid can be predicted based on the melt composition alone or if the T is known independently. If so, Eq. (9) directly relates $X_{Fo}^{ol}$ and $ln(K_{D,Fe^{2+}-Mg})$, and it is straightforward to iterate on $X_{Fo}^{ol}$ to calculate $K_{D,Fe^{2+}-Mg}$. This is the approach used by Herzberg and Asimow (2015) in implementing an olivine–liquid calculation in their PRIMELT program—for each melt composition, T was calculated using Beattie (1993) and the $K_{D,Fe^{2+}-Mg}$ expression in Toplis (2005) was solved iteratively.

Alternatively, Eq. (9) can be rewritten so as to eliminate the composition of olivine from the equation such that the $K_{D,Fe^{2+}-Mg}$ only depends on the liquid composition and temperature. This is done by replacing $X_{Fo}^{ol}$ in Eq. (9) with a temperature and composition dependent expression for either the Mg or $Fe^{2+}$ partition coefficient for olivine–liquid (i.e., $D_{Mg}^{ol/liq}$ or $D_{Fe^{2+}}^{ol/liq}$) and using the stoichiometric constraint that the cation fractions of Mg and Fe in olivine (referred to here as η) equal 2/3, i.e., $X_{Fo}^{ol} = \frac{(D_{Mg}^{ol/liq} X_{Mg}^{liq})}{\eta}$. Note that while we use a value of η = 2/3, which is valid for olivine along the forsterite–fayalite join, η could be adjusted to lower values to account for other divalent cations such as Mn, Ca, and Ni, in the olivine (e.g., Takahashi and Irvine 1981; Beattie 1993).

Putirka et al. (2007) reviewed six olivine–liquid $D_{Mg}^{ol/liq}$ geothermometers and concluded that the expression in Beattie (1993) was the most accurate. The coefficients given in Beattie (1993) were determined using olivine-saturated experimental liquids run over a wide range of P, T, and $fO_2$ (liquid $Fe^{3+}/Fe^{2+}$ ratios were calculated using Kilinc et al. 1983). For internal consistency, we have refit Eq. (10) in Beattie (1993) using our low-$fO_2$ ($n = 201$) data set with liquid $Fe^{3+}/Fe^{2+}$ ratios calculated using Borisov et al. (2018). The equations for $D_{Mg}^{ol/liq}$ and $D_{Fe^{2+}}^{ol/liq}$ are:

$$lnD_{Mg}^{ol/liq} = 0.5(A_{Mg}/T + (P-1)F_{Mg}/T - C_{Mg} - 2ln(1.5NM) - 2ln(3X_{Si}^{liq}) + NF) \quad (11)$$

$$lnD_{Fe^{2+}}^{ol/liq} = 0.5(A_{Fe^{2+}}/T + (P-1)F_{Fe^{2+}}/T - C_{Fe^{2+}} - 2ln(1.5NM) - 2ln(3X_{Si}^{liq}) + NF) \quad (12)$$

where $D_{Mg}^{ol/liq}$ and $D_{Fe^{2+}}^{ol/liq}$ are defined as $(\frac{X_{Mg}^{ol}}{X_{Mg}^{liq}})$ and $(\frac{X_{Fe2+}^{ol}}{X_{Fe2+}^{liq}})$, respectively (as above, the $X_i^{\Phi}$ s are calculated on a single-cation, mole fraction basis); T is in degrees K; P is in bars; and the equations for NM and NF are given in the notes to Table 4. The best-fit values and ± 1σ uncertainties of the coefficients are $A_{Mg} = 13{,}428 \pm 284$; $F_{Mg} = 0.049$; $C_{Mg} = 6.224 \pm 0.191$; $A_{Fe^{2+}} = 12{,}592 \pm 335$; $F_{Fe^{2+}} = 0.048$; and $C_{Fe^{2+}} = 7.916 \pm 0.225$. Note that the pressure terms ($F_{Mg}$ and $F_{Fe2+}$) were taken directly from Beattie (1993) and were not fitted parameters. Supplementary Figure S10 compares the measured vs. predicted values for the n = 201 low-$fO_2$ experiments using Eqs. (11) and (12); both the Mg and $Fe^{2+}$ data are well-described by the equations; however, Eq. (12) systematically overestimates the high-alkali and high-silica chondrite melting experiments (gray circles in Supplementary Figure S10), whereas Eq. (11) does a better job in predicting the partitioning behavior for these experiments. Finally, although written with $D_i^{ol/liq}$ as the dependent variable, both equations were solved for T using a non-linear fitting routine. For each equation, the sum of squared residuals (for T), average ΔT values, and a.a.d. for ΔT and $D_i^{ol/liq}$ are given in Table 4. As noted by earlier authors (e.g., Roeder and Emslie 1970), the fact that the ratio of $A_{Fe2+}$ and $A_{Mg}$ in Eqs. (12) and (11) is close to unity (0.95 for the two equations above) explains the relative insensitivity of $K_{D,Fe^{2+}-Mg}$ to changes in T.

Substituting either Eq. (11) or (12) into Eq. (10) yields an expression for $K_{D,Fe^{2+}-Mg}$ with only one unknown, T (note that T also appears in the $D_i^{ol/liq}$ expressions):

$$\ln K^{ol/liq}_{D,Fe^{2+}-Mg} = \frac{\Delta G^{\circ}}{RT} + \Sigma_j B_j X_j^{liq} + \frac{W^{ol}_{Fe-Mg}}{RT}\left(1 - 2\frac{D^{ol/liq}_{Mg} X^{liq}_{Mg}}{\eta}\right) \quad (13)$$

$$\ln K^{ol/liq}_{D,Fe^{2+}-Mg} = \frac{\Delta G^{\circ}}{RT} + \Sigma_j B_j X_j^{liq} + \frac{W^{ol}_{Fe-Mg}}{RT}\left(1 - 2\left[1 - \frac{D^{ol/liq}_{Fe^{2+}} X^{liq}_{Fe^{2+}}}{\eta}\right]\right) \quad (14)$$

Either of these two equations can be solved iteratively along with either Eq. (11) or (12) to yield a unique value of T and $K_{D,Fe^{2+}-Mg}$ at the olivine liquidus, from which $X^{ol}_{Fo}$ can be determined using either the calculated $K_{D,Fe^{2+}-Mg}$ and the liquid $Mg/Fe^{2+}$, i.e., $X^{ol}_{Fo} = 1/(1 + \frac{K_{D,Fe^{2+}-Mg}}{X^{liq}_{Mg}/X^{liq}_{Fe2+}})$; or the expression $X^{ol}_{Fo} = \frac{(D^{ol/liq}_{Mg} X^{liq}_{Mg})}{\eta}$; or $X^{ol}_{Fo} = 1 - \frac{(D^{ol/liq}_{Fe2+} X^{liq}_{Fe2+})}{\eta}$. Supplementary Section S6 gives additional details of this calculation and a worked example using a representative MORB composition from Gale et al. (2013).

The sets of equations based on $D^{ol/liq}_{Mg}$ and $D^{ol/liq}_{Fe^{2+}}$ perform nearly identically when used to iteratively calculate the T, $X^{ol}_{Fo}$, and $K_{D,Fe^{2+}-Mg}$ for the olivine–liquid pairs in our experimental database (histograms are plotted in Supplementary Figure S11). For the RKD data ($n = 14$) both expressions yield a.a.d. values for temperature (experimental – calculated) of ~ 20 °C; for the complete low-$fO_2$ data set ($n = 201$) the temperature a.a.d. values for the Mg expression and the $Fe^{2+}$ expression are 18 and 23 °C, respectively. For the combined data set, average absolute deviations for calculated $X^{ol}_{Fo}$ and $K_{D,Fe^{2+}-Mg}$ values using the $D^{ol/liq}_{Mg}$ and $D^{ol/liq}_{Fe^{2+}}$ expressions are very similar: $X^{ol}_{Fo}$, 0.0082 vs. 0.0085 and $K_{D,Fe^{2+}-Mg}$, 0.0150 vs. 0.0149, respectively. For reference, the average of the 1σ values for the experimental $X^{ol}_{Fo}$ and $K_{D,Fe^{2+}-Mg}$ values based on the 149 experiments that report errors for Fe and Mg in both phases are 0.0104 and 0.0199, respectively. Thus, the average absolute deviations between the model values and the experimental values are on the same order as the average uncertainties associated with the experimental values. As we have stated above, at $fO_2$ values around IW, calculated $FeO^{liq}$ is insensitive to the choice of $Fe^{3+}/Fe^{2+}$ algorithm. However, this is not the case with increasing $fO_2$ (see Supplementary Figure S1 and Supplementary Section S5). We expect that $D^{ol/liq}_{Mg}$ will be less sensitive to any systematic errors in $Fe^{3+}/Fe^{2+}$ than $D^{ol/liq}_{Fe^{2+}}$, and for this reason we suggest that Eq. (13) be used in preference to Eq. (14).

Note that the $K_{D,Fe^{2+}-Mg}$ calculation is rather insensitive to the cation sum of Mg and $Fe^{2+}$ in the olivine. Lowering η from 2/3 to 0.6600, the median cation sum of $(Fe + Mg)^{ol}$ in the combined low-$fO_2$ data set, only increases the calculated $K_{D,Fe^{2+}-Mg}$ values by, on average, 0.00055 (range = 0.00043–0.00063). Olivine phenocrysts tend to have higher Fe plus Mg cation sums than the olivines in our experimental data set: based on 12,015 high-precision olivine analyses from MORBs and OIBs in Sobolev et al. 2007, $(Fe + Mg)^{ol}$ ranges from 0.6581 to 0.6653 (median = 0.6619) and is essentially uncorrelated with $X^{ol}_{Fo}$. Thus, not explicitly including olivine Ni, Mn, and Ca contents in an $Fe^{2+}$–Mg olivine fractionation or addition calculation will not have a substantial effect on the FeO and MgO contents of the calculated liquids.

## Conclusions

- A set of 1-atm Re wire loop experiments (referred to as "RKD" for Reduced $K_D$,) containing olivine + liquid were run at IW–0.5 or IW + 0.5 on bulk compositions spanning a range of common terrestrial rock types related to Hawai'ian picrite, high-alumina basalt, and MORB. The $Fe^{2+}$–Mg olivine–liquid exchange coefficient, $K^{ol/liq}_{D,Fe^{2+}-Mg}$, varies systematically with liquid and olivine composition in these experiments and the results have been used to contribute to quantifying the compositional dependence of this important parameter. A key feature of the experiments is that the $Fe^{3+}/Fe^*$ ratios of the melts were low ($Fe^{3+}/Fe^* \lesssim 0.04$, Borisov et al. 2018), allowing us to isolate the effects of bulk composition independent of any significant correction for the presence of $Fe^{3+}$ in the quenched glass. This is important, because with increasing $fO_2$, the magnitude of this correction increases and varies (at constant liquid composition, T, and $fO_2$) depending on which $Fe^{3+}/Fe^{2+}$ algorithm is used.
- Fourteen low-$fO_2$ experiments run on pre-saturated Re loops were fit to a version of the model proposed by Toplis (2005), modified using a strictly regular solution model after Ghiorso et al. (1983) to treat the non-ideality of the liquid phase (Eq. (9)). The resulting expression relates $K^{ol/liq}_{D,Fe^{2+}-Mg}$ to T, olivine composition, and melt composition using two fitted parameters: one for the effect of melt $SiO_2$ on the ratio of the activity coefficients of FeO and MgO in the liquid ($B_{Si}$) and one for Fe–Mg mixing in the coexisting olivine ($W^{ol}_{Fe-Mg}$); and a term for ΔG° that was taken from Toplis (2005). This model (Model 1) produces an average absolute deviation in $K^{ol/liq}_{D,Fe^{2+}-Mg}$ for the RKD experiments of 0.0026, which is on order of the analytical precision (1σ ≈ 0.003).
- We combined our RKD data with a literature data set of olivine–liquid pairs from experiments also run at $fO_2 \leq IW + 0.5$ (n = 187) to expand the range of liquid compositions. Applying our modeling approach to this combined data set required two terms in addition to those in Model 1—$B_{Ti}$ and a cross-term, $B_{Si\text{-}(Na+K)}$—to ade-

quately fit the $K^{ol/liq}_{D,Fe^{2+}-Mg}$ values from the literature experiments. This model (Model 2; Eq. (10)) yields an average absolute deviation of 0.0141 in $K^{ol/liq}_{D,Fe^{2+}-Mg}$ between the measured and modeled values for the RKD and literature data ($n = 201$). A key feature of this model is that it captures the significant decreases in $K^{ol/liq}_{D,Fe^{2+}-Mg}$ associated with increasing $TiO_2$ content (up to 18.35 wt%) and total alkalis (up to 8.43 wt%).

- Model 2 gives an expression from which $K^{ol/liq}_{D,Fe^{2+}-Mg}$ can be calculated as a function of T, liquid composition [Si, Ti, and Si-(Na + K)], and coexisting olivine composition. It is more convenient for most applications to calculate an olivine composition given only the liquid composition, T, and $fO_2$ (from which $Fe^{3+}/Fe^{2+}$ in the liquid can be calculated using Borisov et al. 2018). We recast Model 2 as a function of only T and liquid composition assuming the formulation of Beattie (1993) for the T-dependence of olivine–liquid MgO (or FeO) partition coefficients. This eliminates the composition of the coexisting olivine from Eq. (10), thereby making it straightforward to solve for the liquidus temperature for a given melt and the composition of olivine coexisting with the melt at this temperature.

**Supplementary Information** The online version contains supplementary material available at https://doi.org/10.1007/s00410-022-01955-0.

**Acknowledgements** We would like to acknowledge the thoughtful suggestions of Paul Asimow, John Eiler, and Claire Bucholz on an earlier version of this work. The comments of two anonymous reviewers lead to improvements in the manuscript.



## References

Albarède F, Provost A (1977) Petrological and geochemical mass-balance equations: an algorithm for least-square fitting and general error analysis. Comput Geosci 3(2):309–326. https://doi.org/10.1016/0098-3004(77)90007-3

Armstrong JT (1988) Quantitative analysis of silicate and oxide minerals: comparison of Monte Carlo, ZAF, and Φ(ρz) procedures. In: Newbury DE (ed) Microbeam analysis – 1988. San Francisco Press, San Francisco, pp 239–246

Baker MB, Grove TL, Kinzler RJ (1991) Origin of compositional zonation (high-alumina basalt to basaltic andesite) in the Giant Crater Lava Field, Medicine Lake Volcano, Northern California. J Geophys Res 98(B13):21819–21842. https://doi.org/10.1029/91JB01945

Batanova VG, Sobolev AV, Kuzmin DV (2015) Trace element analysis of olivine: high precision analytical method for JEOL JXA-8230 electron probe microanalyzer. Chem Geol 419:149–157. https://doi.org/10.1016/j.chemgeo.2015.10.042

Beattie P (1993) Olivine-melt and orthopyroxene-melt equilibria. Contrib Mineral Petrol 115:103–111. https://doi.org/10.1007/BF00712982

Beckett JR, Mendybaev RA (1997) The measurement of oxygen fugacities in flowing gas mixtures at temperatures below 1200 °C. Geochim Cosmochim Acta 61(20):4331–4336. https://doi.org/10.1016/S0016-7037(98)00212-9

Bédard JH (2005) Partitioning coefficients between olivine and silicate melts. Lithos 83(3–4):394–419. https://doi.org/10.1016/j.lithos.2005.03.011

Berry AJ, O'Neill HSC (2022) Oxygen content, oxygen fugacity, the oxidation state of iron, and mid-ocean ridge basalts. In: Moretti R, Neuville RD (Ed) Magma Redox Geochemistry, Geophysical Monograph Series, American Geophysical Union pp. 155–164. https://doi.org/10.1002/9781119473206.ch8

Blundy J, Melekhova E, Ziberna L, Humphreys MCS, Cerantola V, Brooker RA, McCammon CA, Pichavant M, Ulmer P (2020) Effect of redox on Fe-Mg-Mn exchange between olivine and melt and an oxybarometer for basalts. Contrib Mineral Petrol. https://doi.org/10.1007/s00410-020-01736-7

Borisov AA, Jones JH (1999) An evaluation of Re, as an alternative to Pt, for the 1 bar loop technique: an experimental study at 1400 °C. Am Mineral 84:1528–1534. https://doi.org/10.2138/am-1999-1006

Borisov AA, Shapkin AI (1989) New empiric equation of dependence of $Fe^{3+}/Fe^{2+}$ ratio in natural Melts on their composition, oxygen fugacity and temperature. Geokhimiya 6:892–897

Borisov AA, Behrens H, Holtz F (2018) Ferric/ferrous ratio in silicate melts: a new model for 1 atm data with special emphasis on the effects of melt composition. Contrib Mineral Petrol. https://doi.org/10.1007/s00410-018-1524-8

Bowen NL, Schairer JF (1935) The system MgO-FeO-$SiO_2$. Am J Sci. https://doi.org/10.1007/s00410-018-1524-8

Brown Krein S, Molitor ZJ, Grove TL (2021) ReversePetrogen: A multiphase dry reverse fractional crystallization-mantle melting thermobarometer applied to 13,589 mid-ocean ridge basalt glasses. J Geophys Res. https://doi.org/10.1029/2020JB021292

Carmichael ISE (1991) The redox states of basic and silicic magmas: a reflection of their source regions? Contrib Mineral Petrol 106:129–141

Collinet M, Grove TL (2020) Widespread production of silica- and alkali-rich melts at the onset of planetisimal melting. Geochim Cosmochim Acta 277:334–357. https://doi.org/10.1016/j.gca.2020.03.005

Cottrell E, Birner SK, Brounce M, Davis FA, Waters LE, Kelley KA (2022) Oxygen fugacity across tectonic settings. In: Moretti R, Neuville RD (Ed), Magma Redox Geochemistry, Geophysical Monograph Series, American Geophysical Union pp. 33–61. https://doi.org/10.1002/9781119473206.ch3

Danyushevsky LV, Sokolov S, Falloon TJ (2002) Melt inclusions in olivine phenocrysts: using diffusive re-equilibration to determine the cooling history of a crystal, with implications for the origin of

olivine-phyric volcanic rocks. J Petrol 43(9):1651–2167. https://doi.org/10.1093/petrology/43.9.1651
Davis FA, Cottrell E (2018) Experimental investigation of basalt and peridotite oxybarometers: implications for spinel thermodynamic models and $Fe^{3+}$ compatibility during generation of upper mantle melts. Am Mineral 103(7):1056–1067. https://doi.org/10.2138/am-2018-6280
Delano JW (1980) Chemistry and liquidus phase relations of Apollo 15 red glass: implications for the deep lunar interior. Proc Lunar Sci Conf 11:251–288
Donovan JJ, Tingle TN (1996) An improved mean atomic number background correction for quantitative microanalysis. Microsc Microanal 2(1):1–7. https://doi.org/10.1017/S1431927696210013
Falloon TJ, Danyushevsky LV, Ariskin A, Green DH, Ford CE (2007) The application of olivine geothermometry to infer crystallization temperatures of parental liquids: implications for the temperature of MORB magmas. Chem Geol 241(3–4):207–233. https://doi.org/10.1016/j.chemgeo.2007.01.015
Filiberto J, Dasgupta R (2011) $Fe^{2+}$-Mg partitioning between olivine and basaltic melts: applications to genesis of olivine-phyric shergottites and conditions of melting in the Martian interior. Earth Planet Sci Lett 304(3–4):527–537. https://doi.org/10.1016/j.epsl.2011.02.029
Ford CE, Russell DG, Craven JA, Fisk MR (1983) Olivine-liquid equilibria: temperature, pressure, and composition dependence of the crystal/liquid cation partition coefficients for Mg, $Fe^{2+}$. Ca and Mn J Petrol 24(3):256–266. https://doi.org/10.1093/petrology/24.3.256
French BM, Eugster HP (1965) Experimental control of oxygen fugacities by graphite-gas equilibriums. J Geophys Res 70(6):1529–1539
Gaetani GA, Watson EB (2002) Modeling the major-element evolution of olivine-hosted melt inclusions. Chem Geol 183(1–4):25–41. https://doi.org/10.1016/S0009-2541(01)00370-9
Gale A, Dalton CA, Langmuir CH, Su Y, Schilling J-G (2013) The mean composition of ocean ridge basalts. Geochem, Geophys, Geosyst 14(3):489–518. https://doi.org/10.1029/2012GC004334
Gale A, Langmuir CH, Dalton CA (2014) The global systematics of ocean ridge basalts and their origin. J Petrol 55(6):1051–1082. https://doi.org/10.1093/petrology/egu017
Gee LL, Sack RO (1988) Experimental petrology of melilite nephelinites. J Petrol 29(6):1233–1255. https://doi.org/10.1093/petrology/29.6.1233
Ghiorso MS, Kress VC (2004) An equation of state for silicate melts. II. Calibration of volumetric properties at $10^5$ Pa. Am J Sci 304(8–9):679–751. https://doi.org/10.2475/ajs.304.8-9.679
Ghiorso MS, Sack RO (1995) Chemical mass transfer in magmatic processes IV. A revised and internally consistent thermodynamic model for the interpolation and extrapolation of liquid-solid equilibria in magmatic systems at elevated temperatures and pressures. Contrib Mineral Petrol 119:197–212. https://doi.org/10.1007/BF00307281
Ghiorso MS, Carmichael ISE, Rivers ML, Sack RO (1983) The Gibbs free energy of mixing of natural silicate liquids; an expanded regular solution approximation for the calculation of magmatic intensive variables. Contrib Mineral Petrol 84:107–145. https://doi.org/10.1007/BF00371280
Grove TL (1982) Use of Fe-Pt alloys to eliminate the iron loss problem in 1 atmosphere gas mixing experiments: theoretical and practical considerations. Contrib Mineral Petrol 78:298–304. https://doi.org/10.1007/BF0039892
Grove TL, Beaty DW (1980) Classification, experimental petrology and possible volcanic histories of the Apollo 11 high-K basalts. Proc Lunar Sci Conf 11:149–177
Grove TL, Brown SM (2018) Magmatic processes leading to compositional diversity in igneous rocks: Bowen (1928) revisited. Am J Sci 318:1–28. https://doi.org/10.2475/01.2018.02
Grove TL, Juster TC (1989) Experimental investigation of low Ca pyroxene stability and olivine-pyroxene-liquid equilibria at 1-atm in natural basaltic and andesitic liquids. Contrib Mineral Petrol 103:287–305. https://doi.org/10.1007/BF00402916
Herzberg C, Asimow PD (2015) PRIMELT3 MEGA.XLSM software for primary magma calculation: Peridotite primary magma MgO contents from the liquidus to the solidus. Geochem, Geophys, Geosyst 16(2):563–578. https://doi.org/10.1002/2014GC005631
Herzberg C, O'Hara MJ (1998) Phase equilibrium constraints on the origin of basalts, picrites, and komatiites. Earth Sci Rev 44(1–2):39–79. https://doi.org/10.1016/S0012-8252(98)00021-X
Herzberg C, O'Hara MJ (2002) Plume-associated ultramafic magmas of Phanerozoic age. J Petrol 43(10):1857–1883. https://doi.org/10.1093/petrology/43.10.1857
Hess PC (1971) Polymer model of silicate melts. Geochim Cosmochim Acta 35(3):289–306. https://doi.org/10.1016/0016-7037(71)90038-X
Hess PC (1992) Phase equilibria constraints on the origin of ocean floor basalts. In Mantle Flow and Melt Generation at Mid-Ocean Ridges, Geophysical Monograph 71, edited by Blackman D, Morgan JP, Sinton J, American Geophysical Union pp. 67–102
Hirschmann MM, Baker MB, Stolper EM (1998) The effect of alkalis on the silica content of mantle-derived melts. Geochim Cosmochim Acta 62(5):883–902. https://doi.org/10.1016/S0016-7037(98)00028-3
Houlier B, Cheraghmakani M, Jaoul O (1990) Silicon diffusion in San Carlos olivine. Phys Earth Planet Inter 62(3–4):329–340. https://doi.org/10.1016/0031-9201(90)90177-Y
Huebner JS (1971) Buffering techniques for hydrostatic systems at elevated pressures. Research techniques for high pressure and high temperature, Ed: Ulmer GC, Springer, Berlin, Heidelberg pp. 123–177
Jarosewich E, Nelen JA, Norberg JA (1979) Electron microprobe reference samples for mineral analyses. Smithsonian Contribut Earth Sci Mineral Sci Investig 1976–1977(22):68–73
Jayasuriya KD, O'Neill HSC, Berry AJ, Campbell SJ (2004) A Mössbauer study of the oxidation state of Fe in silicate melts. Am Mineral 89(11–12):1597–1609
Jochum KP, Stoll B, Herwig K, Wilbold M, Hofmann AW, Amini M et al (2006) MPI-DING reference glasses for in situ microanalysis: New reference values for element concentrations and isotope ratios. Geochem Geophys Geosyst 7(2):1–44. https://doi.org/10.1029/2005GC001060
Jones JH (1988) Partitioning of Mg and Fe between olivine and liquids of lunar compositions: the roles of composition, pressure, and Ti speciation. Proc Lunar Sci Conf 19:561–562
Kessel R, Beckett JR, Stolper EM (2001) Thermodynamic properties of the Fe-Pt system. Am Mineral 86(9):1003–1014. https://doi.org/10.2138/am-2001-8-907
Kilinc A, Carmichael ISE, Rivers ML, Sack RO (1983) The ferric-ferrous ratio of natural silicate liquids equilibrated in air. Contrib Mineral Petrol 84:136–140. https://doi.org/10.1007/BF00373086
Kress VC, Carmichael ISE (1988) Stoichiometry of the iron oxidation reaction in silicate melts. Am Mineral 73(11–12):1267–1274
Kress VC, Carmichael ISE (1991) The compressibility of silicate liquids containing Fe2O3 and the effect of composition, temperature, oxygen fugacity and pressure on their redox states. Contrib Mineral Petrol 108:82–92. https://doi.org/10.1007/BF00307328
Kushiro I (1975) On the nature of silicate melt and its significance in magma genesis: regularities in the shift of the liquidus boundaries involving olivine, pyroxene, and silica minerals. Am J Sci 275:411–431
Kushiro I, Mysen BO (2002) A possible effect of melt structure on the Mg-$Fe^{2+}$ partitioning between olivine and melt. Geochim Cosmochim Acta 66(12):2267–2272. https://doi.org/10.1029/98GL01844

Kushiro I, Walter MJ (1998) Mg-Fe partitioning between olivine and mafic-ultramafic melts. Geophys Res Lett 25(13):2337–2340. https://doi.org/10.2475/ajs.275.4.411

Lambart S, Hamilton S, Lang OI (2022) Compositional variability of San Carlos olivine. Chem Geol 605:120968. https://doi.org/10.1016/j.chemgeo.2022.120968

Le Maitre RW (1976) The chemical variability of some common igneous rocks. J Petrol 17(4):589–598. https://doi.org/10.1093/petrology/17.4.589

Llovet X, Salvat F (2017) PENEPMA: a Monte Carlo program for the simulation of X-ray emission in electron probe microanalysis. Microsc Microanal 23(3):634–646. https://doi.org/10.1017/S1431927617000526

Longhi JW, D, Hays JF, (1978) The distribution of Fe and Mg between olivine and lunar basaltic liquids. Geochim Cosmochim Acta 42(10):1545–1558. https://doi.org/10.1016/0016-7037(78)90025-X

Matzen AK, Baker MB, Beckett JR, Stolper EM (2011) Fe-Mg partitioning between olivine and high-magnesian melts and the nature of Hawaiian parental liquids. J Petrol 52(7–8):1243–1263. https://doi.org/10.1093/petrology/egq089

Mills KC, Yuan L, Li Z, Zhang GH, Chou KC (2012) A review of the factors affecting the thermophysical properties of silicate slags. High Temp Mater Processes (london) 31(4–5):301–321. https://doi.org/10.1515/htmp-2012-0097

Mysen BO (1990) Relationships between silicate melt structure and petrologic processes. Earth Sci Rev 27(4):281–365. https://doi.org/10.1016/0012-8252(90)90055-Z

Mysen BO (2006) Redox equilibria of iron and silicate melt structure: implications for olivine/melts element partitioning. Geochim Cosmochim Acta 70(12):3121–3138. https://doi.org/10.1016/j.gca.2006.03.014

Mysen BO, Dubinsky EV (2004) Melt structural control on olivine/melt element partitioning of Ca and Mn. Geochim Cosmochim Acta 68(7):1617–1633. https://doi.org/10.1016/j.gca.2003.09.010

Mysen BO, Shang J (2005) Evidence from olivine/melt element partitioning that nonbridging oxygen in silicate melts are not equivalent. Geochim Cosmochim Acta 69(11):2861–2876. https://doi.org/10.1016/j.gca.2004.12.028

Mysen BO, Virgo D, Seifert FA (1982) The structure of silicate melts: implications for chemical and physical properties of natural magma. Rev Geophys 20(3):353–383. https://doi.org/10.1029/RG020i003p00353

Nikolaev GS, Borisov AA, Ariskin AA (1996) Calculation of the ferric-ferrous ratio in magmatic melts: testing and additional calibration of empirical equations for various magmatic series. Geochem Int 34(8):641–649

O'Hara MJ (1968) The bearing of phase equilibria studies in synthetic and natural systems on the origin and evolution of basic and ultrabasic rocks. Earth Sci Rev 4:69–133

O'Neill HSC, Pownceby MI, McCammon CA (2003) The magnesiowüstite iron equilibrium and its implications for the activity-composition relations of (Mg, $Fe_)2Si_O4$ olivine solid solutions. Contrib Mineral Petrol 146:308–325. https://doi.org/10.1007/s00410-003-0496-4

O'Neill HSC, Berry AJ, Mallmann G (2018) The oxidation state of iron in Mid-Ocean Ridge Basaltic (MORB) glasses: implications for their petrogenesis and oxygen fugacties. Earth Planet Sci Lett 504:152–162. https://doi.org/10.1016/j.epsl.2018.10.002

O'Neill HSC (2022) The thermodynamic controls of sulfide saturation in silicate melts. In: Moretti R, Neuville RD, (Ed), Magma Redox Geochemistry, Geophysical Monograph Series, American Geophysical Union: pp. 177–213. https://doi.org/10.1002/9781119473206.ch10

Partzsch GM, Lattard D, McCammon C (2004) Mössbauer spectroscopic determination of $Fe^{3+}/Fe^{2+}$ in synthetic basaltic glass: a test of empirical $fO_2$ equations under superliquidus, and subliquidus conditions. Contrib Mineral Petrol 147:565–580. https://doi.org/10.1007/s00410-004-0571-5

Putirka KD (2016) Rates and styles of planetary cooling on Earth, Moon, Mars, and Vesta, using new models for oxygen fugacity, ferric-ferrous ratios, olivine-liquid Fe-Mg exchange, and mantle potential temperature. Am Mineral 101:819–840. https://doi.org/10.2138/am-2016-5402

Putirka KD, Perfit M, Ryerson FJ, Jackson MG (2007) Ambient and excess mantle temperatures, olivine thermometry, and active vs. passive upwelling. Chem Geol 241(3–4):177–206. https://doi.org/10.1016/j.chemgeo.2007.01.014

Reynolds JR, Langmuir CH (1997) Petrological systematics of the Mid-Atlantic Ridge south of Kane: Implications for ocean crust formation. J Geophys Res 102(B7):14915–14946. https://doi.org/10.1029/97JB00391

Robie RA, Hemingway BS, Fisher JR (1979) Thermodynamic properties of minerals and related substances at 298.15K and 1 bar (105 pascals) pressure and at higher temperatures. U.S. Geological Survey Bulletin 1452

Roeder PL (1974) Activity of iron and olivine solubility in basaltic liquids. Earth Planet Sci Lett 23:397–410. https://doi.org/10.1016/0012-821X(74)90129-0

Roeder PL, Emslie RF (1970) Olivine-liquid equilibrium. Contrib Mineral Petrol 29:275–289. https://doi.org/10.1007/BF00371276

Ryerson FJ (1985) Oxide solution mechanisms in silicate melts: systematic variations in the activity coefficient of $SiO_2$. Geochim Cosmochim Acta 49(3):637–649. https://doi.org/10.1016/0016-7037(85)90159-0

Sack RO, Carmichael ISE, Rivers M, Ghiorso MS (1980) Ferric-ferrous equilibria in natural silicate liquids at 1 bar. Contrib Mineral Petrol 75:369–376. https://doi.org/10.1007/BF00374720

Shi P (1993) Low pressure phase relationships in the system $Na_2O$-CaO-FeO-MgO-$Al_2O_3$-$SiO_2$ at 1100 °C, with implications for the differentiation of basaltic magmas. J Petrol 34(4):743–762. https://doi.org/10.1093/petrology/34.4.743

Snyder DA, Carmichael ISE (1992) Olivine-liquid equilibria and the chemical activities of FeO, NiO, $Fe_2O_2$, and MgO in natural basic melts. Geochim Cosmochim Acta 56(1):303–318. https://doi.org/10.1016/0016-7037(92)90135-6

Sobolev AV, Hofmann AW, Kuzmin DV, Yaxley GM, Arndt NT, Chung S-L, Danyushevsky LV, Elliott T, Frey FA, Garcia MO, Gurenka AA, Kamanetsky VS, Kerr AC, Krivolutskaya NA, Matvienklov VV, Nikogosian IK, Rocholl A, Sigurdsson IA, Sushchevskaya NM, Teklay M (2007) The amount of recycled crust in sources of mantle-derived melts. Science 316:412–417. https://doi.org/10.1126/science.1138113

Spandler C, O'Neill HSC (2010) Diffusion and partition coefficients of minor and trace elements in San Carlos olivine at 1,300 °C with some geochemical implications. Contrib Mineral Petrol 159:791–818. https://doi.org/10.1007/s00410-009-0456-8

Stixrude L, Lithgow-Bertelloni C (2012) Geophysics of chemical heterogeneity in the mantle. Annu Rev Earth Planet Sci 40:569–595

Stolper EM, Sherman S, Garcia MO, Baker MB, Seaman C (2004) Glass in the submarine section of the HSDP2 drill core, Hilo, Hawaii. Geochem Geophys Geosyst. https://doi.org/10.1029/2003GC000553

Takahashi E, Irvine TN (1981) Stoichiometric control of crystal/liquid single-component partition coefficients. Geochim Cosmochim Acta 45(7):1181–1185. https://doi.org/10.1016/0016-7037(81)90141-1

Thornton CP, Tuttle OF (1960) Chemistry of igneous rocks: I. Differentiation index. J Sci 258:664–668. https://doi.org/10.2475/ajs.258.9.664

Tollan PME, O'Neill HSC, Hermann J (2018) The role of trace elements in controlling H incorporation in San Carlos olivine. Contrib Mineral Petrol. https://doi.org/10.1007/s00410-018-1517-7

Toplis MJ, Libourel G, Carroll MR (1994) The role of phosphorus in crystallization processes of basalt: an experimental study. Geochim Cosmochim Acta 58(2):797–810

Toplis MJ (2005) The thermodynamics of iron and magnesium partitioning between olivine and liquid: criteria for assessing and predicting equilibrium in natural and experimental systems. Contrib Mineral Petrol 149:22–39. https://doi.org/10.1007/s00410-004-0629-4

Tuff J, O'Neill HSC (2010) The effect of sulfur on the partitioning of Ni and other first-row transition elements between olivine and silicate melt. Geochim Cosmochim Acta 74(21):6180–6205. https://doi.org/10.1016/j.gca.2010.08.014

Ulmer P (1989) The dependence of the $Fe^{2+}$-Mg cation-partitioning between olivine and basaltic liquid on pressure, temperature and composition. Contrib Mineral Petrol 101:261–273. https://doi.org/10.1007/BF00375311

Wadhwa M (2008) Redox conditions on small bodies, the moon and Mars. Rev Mineral Geochem 68:493–510. https://doi.org/10.2138/rmg.2008.68.17

Warren JM (2016) Global variations in abyssal peridotite compositions. Lithos 248–251:193–219

Waters LE, Cottrell E, Coombs ML, Kelley KA (2020) Generation of calc-alkaline magmas during crystallization at high oxygen fugacity: an experimental and petrologic study of tephras from Buldir Volcano, Western Aleutian Arc, Alaska, USA. J Petrol. https://doi.org/10.1093/petrology/egaa104

Watson EB (1982) Basalt contamination by continental crust: some experiments and models. Contrib Mineral Petrol 80(1):70–87. https://doi.org/10.1007/BF00376736

Wiser NM, Wood BJ (1991) Experimental determination of activities in Fe-Mg olivine at 1400 K. Contrib Mineral Petrol 108:146–153. https://doi.org/10.1007/BF00307333

Xirouchakis D, Hirschmann MM, Simpson JA (2001) The effect of titanium on the silica content and on mineral-liquid partitioning of mantle-equilibrated melts. Geochim Cosmochim Acta 65(14):2201–2217. https://doi.org/10.1016/S0016-7037(00)00549-4